Quantitative Analysis of 3D Heterochromatin Structures Within and Between Neuronal Cell Types

by

Rory Smith

A THESIS SUBMITTED IN PARTIAL FULFILMENT
OF THE REQUIREMENTS FOR THE DEGREE OF
BACHELOR OF SCIENCE (HONOURS)

in the Department of

BIOLOGY, NEUROBIOLOGY
UNIVERSITY OF VICTORIA

We accept this thesis as conforming to the required standard

We acknowledge and respect the Lək̓ʷəŋən peoples on whose traditional territory the University of Victoria stands, and the Songhees, Esquimalt and W̱SÁNEĆ peoples whose historical relationships with the land continue to this day.

Quantitative Analysis of 3D Heterochromatin Structures Within and Between Neuronal Cell Types

by

Rory Smith

Supervisory Committee

Dr. Kerry R. Delaney

List of Abbreviations

GFP	Green Fluorescent Protein
RT	Rett Syndrome
WT	Wild Type
CDF	Cumulative Density Function
CDH	Cumulative Density Histogram
KDE	Kernel Density Estimated
RMS	Root-Mean Square (distance)

Acknowledgements

Many thanks to Dr. Delaney for the opportunity to undertake this project, and especially for the invaluable lessons on how to think critically and independently.

I also thank Dr. Chow for taking the time to teach me the practical use of the microscope and also to develop a deeper understanding of its underlying principles.

Special thanks to Tariq Nashmi for his excellent work in brain slicing and, alongside Vasil Kecheliev, for fostering such a positive atmosphere in the lab. I am also grateful to Dr. Raad Nashmi and Giselle for providing an ACh brain for my project. I also truly appreciated Giselle's anatomical expertise in helping me identify brain regions accurately.

I also really appreciate my Honour's comrades Riya and Emir for being supportive and direct with feedback.

I also want to thank the rest of my Biology friends who made the last few years of my degree really memorable.

List of Figures

Chapter 0: Abstract

Heterochromatin organization within neuronal nuclei plays a critical role in maintaining genomic stability and regulating gene expression, yet its 3D morphological variability between neuron types remains poorly understood. Using confocal microscopy, we quantitatively analyzed heterochromatin 3D structures within neuronal nuclei. Existing methods in the literature were re-created to measure the distribution of nuclear intensity into predefined classes, as well as basic morphological features of the foci (volume, eccentricity, etc.). However, these morphological descriptors impose rigid, preconceived geometric assumptions that do not consider 3D spatial positioning. We attempt to address these limitations with a novel computational method that directly assays both spatial and morphological "similarity" of heterochromatin formations in nuclei. This approach was applied to a range of neuron types to assess variation within and between groups. Our results demonstrate significant differences between spatial heterochromatin foci positioning between neural types. If coupled with immunohistochemistry and increased replicates, we conclude with a demonstration of how this analysis could be applied to effectively study single-genotype differences in heterochromatin formation. This methodology offers a generalizable framework for studying morphological changes in other genotypes and nuclear protein disorders, which is of interest to various neurodevelopmental disorders.

Chapter 1.0: Introduction

The concept of morphologically distinct neurons was first formalized in the late 19th century by Santiago Ramón y Cajal through the Neuron Doctrine. At a time when the dominant belief held that the nervous system was a continuous, reticulated network, Cajal argued instead that neurons are discrete, autonomous units that communicate across synapses (Rozo et al., 2024). Using Golgi's silver staining technique, he produced detailed anatomical drawings that revealed an unexpected diversity in neuronal shapes and structures across the brain (Rozo et al., 2024). This morphological variety pointed to a deeper principle: that different neuron types might serve specialized roles within neural circuits.

The Neuron Doctrine laid the foundation for modern neuroscience by reframing the neuron as the fundamental unit of the nervous system. Today, however, this doctrine is interpreted through a hermeneutic of epigenetic complexity (Qureshi et al., 2014). Morphology remains relevant, but advances in electrophysiology, high-resolution imaging, and single-cell transcriptomics have added new dimensions to how neuronal identity is defined and understood (McKiernan et al., 2017). In particular, the insight from these tools emphasise a continuous spectrum of neuronal identity; as molecular markers cluster, not coincide (McKiernan et al., 2017). More importantly, these tools have emphasized that a neuron's identity is not determined by its structure or location, but by the specific patterns of gene expression it maintains (Cembrowski et al., 2016).

In this modern framework, neuronal classification is increasingly guided by gene expression profiles - what a neuron turns on or off - rather than by its external morphology. This shift marks a move away from inferring neuronal identity from their silhouette to the readout of an assay. However, we have to consider that genes are not randomly scattered within the nucleus; their 3D positioning affects their accessibility, activity, and timing of expression (Zagirova et al., 2024). This spatial organization plays a regulatory role, inducing each neuron type to express a distinct set of genes. A broad outline of nuclear organization can be seen with DAPI, which - much like the Golgi stain - offers a limited but revealing glimpse into large structural features. This approach may still help correlate 3D architecture to function, honouring Cajal's approach in an era of epigenetic complexity.

1.1: Different Neurons Types Express Different Genes

Layer 2 of the mammalian cortex is largely composed of excitatory pyramidal neurons, which are glutamatergic, spiny, and are important for modulating processing deeper in the cortex (Weiler et al., 2023; Quiquempoix et al., 2018). These pyramidal neurons serve as key hubs for interareal (between cortical regions) and intracortical communication (Weiler et al., 2023). Their projections can go so far that they commissure across hemispheres (Robles et al., 2020). Layer 2 interneurons extend their dendrites towards layer 1, integrating modulatory signals (Weiler et al., 2023). Layer 2/3 also contains a diverse population of inhibitory interneurons (Kepecs and Fishell, 2014). Among these are the parvalbumin-positive (PV^+) interneurons which are fast-spiking basket cells that primarily target the perisomatic region of pyramidal neurons, exerting control over spike timing and synchrony (Kepecs and Fishell, 2014).

The CA1 region of the hippocampus, a key area for memory encoding and spatial navigation, serves as the primary output node (Kandel et al., 2021). CA1 pyramidal neurons- like those in layer 2 and deeper cortical areas- are excitatory, glutamatergic cells characterized by a prominent apical dendrite extending through the stratum radiatum, where they receive input from CA3 pyramidal neurons (Nielsen et al., 2013). These neurons can be distinguished from other hippocampal and cortical subtypes by the expression of markers such as *Bcl11b* and Zbtb20, which has a role in determining its cell fate from other isocortex identities **(**Nielsen et al., 2013). Functionally, CA1 pyramidal neurons in rats can be divided into two mutually exclusive populations based on receptor expression for acetylcholine and glutamate (Graves et al., 2012). Horowitz et. al (2019) have used the term “extreme neuroplasticity” to describe the changes in these neurons' functional and morphological properties that vary with activity as well as stage of life cycle.

Medium spiny neurons (MSNs) are the main projection neurons of the striatum of the Basal Ganglia- a brain region essential for action selection, motivation, and reward. MSNs comprise about 90–95% of neurons in the striatum and are GABAergic (Lanciego et. al, 2012). They have dense, spiny dendrites that receive excitatory input from the cortex, thalamus, and limbic structures (Lanciego et. al, 2012). Their projections initiate motor signals by synapsing onto regions such as the Globus Pallidus and Substantia Nigra Pars Reticulata. In general, MSN s can be sub-categorized by whether they express the D1 or D2 receptor, which respond in opposite ways to the neurotransmitter dopamine (Nishi et. al, 2011). D1-MSN’s and D2-MSN’s also associate with different synaptic targets, comprising the “direct” and “indirect” pathway respectively (Nishi et. al, 2011). D1 make MSN’s excited by dopamine, while D2 inhibits MSNs. Besides the MSN’s, a minority of striatum neurons express ACh and are noticeably larger (Lanciego et. al, 2012).

Within the cerebellum, the enormous dendritic arbor of GABAergic Purkinje neurons (Takeo et. al, 2021; Paul et. al, 2022) make them unmistakable from their neighbors. As the sole output of the cerebellum, they play a critical role in motor coordination, fine-tuning motor commands in response to incoming sensory signals (Kandel et al., 2021). Purkinje neurons are continuously learning through Long Term Depression, which initiates the process of remodeling its dendritic arbor to reshuffle its some 100,000 synaptic connections (Hoxha et al., 2016). The rearrangement of the dendrites requires complex coordination of actin localization, which is done through the Lhx1/5 pathway and Espin (Lui e. al., 2017). The ability of Purkinje cells to undergo long-term depression (LTD) at the parallel fiber synapse—a mechanism of neuronal learning—is mediated by a biochemical cascade involving mGluR1 (metabotropic glutamate receptor 1), PKCα (protein kinase C alpha), GluR2 (AMPA receptor subunit), and PICK1 (protein interacting with C kinase 1) (Hirano et al., 2013). Purkinje neurons undergo tremendous amounts of DNA transcription and protein translation to maintain their arbor, and this is reflected by the high density of nuclear pores (Baltanas et al., 2011)

The extraordinary diversity of neuronal types - reflected in their morphology, connectivity, and electrophysiological properties - forms the structural and functional basis of complicated brain circuits. How neurons are differentiated into subtypes is thus an important basic research question. One such way involves chromatin structure- which determines which genes are accessible, active, or silenced. When these regulatory processes break down, the consequences can be profound—disrupting neuronal function and contributing to neurodevelopmental disorders. Thus, a key area of research is understanding how chromatin structure, particularly heterochromatin, contributes to neuronal identity and stability.

Chapter 1.2: chromatin

Chromatin is a DNA-protein complex that has a profound role in regulating cell-type specific gene expression. Chromatin regulates genes by condensing DNA into inaccessible structures, effectively “hiding” it from the cell, and preventing transcription. When chromatin is condensed it is called Heterochromatin, and when uncondensed, chromatin is called

Euchromatin (Loyfer et al., 2023). Heterochromatin creates cell specific gene expression patterns mostly by turning genes “off”, rather than by turning them “on”; The structure of chromatin is both a facilitator and hallmark of cell identity and function (Smith and Meissner, 2013; Lyons et al., 2013).

At its most basic, chromatin consists of DNA wrapped around a cluster of 8 histones, which is called a nucleosome (Kouzarides et al., 2007). In Euchromatin, these nucleosomes appear in a “beads-on-a-string” configuration, where each nucleosome is separated by approximately 147 base pairs of DNA (Baldi et al., 2020; Kouzarides et al., 2007). When inhibitory heterochromatin forms, these “beads on a string” coalesce into a tight mass, physically restricting transcriptional proteins from accessing them (Baldi et al., 2020).

The composition of histones in chromatin plays a major role in determining whether a region will form into euchromatin or heterochromatin. There is a wide array of histone types, as well as post-translational modifications, that influence the chromatin structure and its transcriptional activity. For example, tri-methylation of lysine 4 on histone H3 (H3K4me3) is generally associated with active euchromatin and gene transcription, while tri-methylation of lysine 27 on histone H3 (H3K27me3) is linked to repressive heterochromatin formation (Bannister and Kouzarides, 2011; Loyfer et al., 2023). Similarly, acetylation of lysine residues such as H3K9ac and H3K27ac correlates with transcriptional activation by loosening chromatin structure and promoting accessibility to transcription factors (Bannister and Kouzarides, 2011). In contrast, methylation of H3K9 (e.g., H3K9me3) is a hallmark of constitutive heterochromatin and is associated with gene silencing (Schor et al., 2009).

Chapter 1.3: Sub-Microscopic 3D Heterochromatin Architecture

In addition to modulating gene accessibility, chromatin organizes into higher-order structures that regulate gene expression. One key structure is the chromatin loop, which brings distant regulatory elements - such as enhancers and promoters - into close physical proximity to facilitate transcription (Martino et al., 2023; Wilczynski et al., 2013). These loops are formed by proteins like CTCF, which defines loop boundaries, and Cohesin, which extrudes and “ties off” the loop (Cai and Wang, 2023; Fujita et al., 2022).

Chromatin loops are crucial for neural differentiation. A well-characterized example is the regulation of SOX2, which is involved in keeping neuronal progenitors in a replicative, mitotic state until many neurons have formed (Favoro et al., 2009). Its expression depends on chromatin loops that bring regulatory elements into contact (Wei et al., 2010). Disruption of the loop forming process reduces *SOX2* expression, leading to fewer neurons in the adult brain (Martino et al., 2023). Chromatin loops are also essential for responding to external signaling cues and inducing developmentally appropriate gene expression, including those for growth and maintenance of neurons (Abewe et al., 2025; Hirayama et. al, 2022; Lbarra et al., 2022).

Another level of nuclear architecture is chromosome territories, where entire chromosomes occupy distinct nuclear regions. These spatial arrangements influence gene accessibility and vary by cell type and disease state (Favoro et al., 2009). Moreover, these arrangements vary by species (Tanabe et. al, 2002), cell type, and even disease state (Finlan et. al, 2008). It has also been suggested that chromosome territories persist to maintain cell type specification (Zagirova et al., 2024).

Another layer of genome organization involves Lamina-Associated Domains (LADs), which are regions of the genome that interact with the nuclear lamina at the membrane of the nucleus (Wilczynski et al., 2013). LADs typically contain DNA that is actively transcriptionally repressed. In differentiated cells like neurons, inactive and heterochromatic regions are often positioned in LADs, contributing to cell-type-specific gene expression patterns (Kriukov et al., 2024). Both cortical neurons and Purkinje neurons actively use Lamin at different stages of development, and a deficit has been shown to disrupt the “inverted nuclear architecture” characteristic of the retinal rod cells (Solovei et al., 2013). Their positioning is influenced by the proportion of nucleotides that are A/T content, and can shift during development and ageing, correlating with changes in gene expression (Meuleman et al., 2013).

Chapter 1.4: Heterochromatin Foci

Heterochromatin often organizes into distinct and spatially distributed foci which appear as spherical structures under the microscope (Ito Ishoda et al., 2022; Brandle et al., 2022). These foci vary in number, shape, and positioning from cell to cell, but are typically found near the nuclear periphery or adjacent to the nucleolus. Studies have demonstrated that most of the DNA that makes up the foci are pericentromeric, meaning near the centromere, and composed of “Satellite DNA”- which are short sequences repeated thousands of times (Brandle et al., 2022). Although considered part of the “dark genome” due to their non-coding nature, satellite sequences are known to play critical roles in maintaining large scale genome structure and stability (Packiaraj et al., 2024; Brandle et al., 2022). These regions are also enriched in sequence-specific DNA-binding proteins, and the histone modification H3K9me3 (Montavon et al., 2021; Brandle et al., 2022).

Similar to the phase condensate model proposed for nucleoli (Brangwynne et al., 2011), recent work has increasingly supported the idea that heterochromatin foci are formed via liquid-liquid phase separation interactions. According to Zhang et al. (2023), heterochromatin exhibits many features characteristic of phase-separated condensates, including dynamic fusion, spherical shape, and rapid internal molecular exchange. The model helps explain how heterochromatin domains can exist as distinct yet membrane-less compartments within the nucleus (Strom et al., 2017). Strom et al. (2017) also show that as heterochromatin foci mature, they become less perfectly spherical. This change in shape is linked to decreased fusing of foci (Zhang et al., 2023), and increased amounts of DNA and nucleosomes being incorporated into the domains, along with tighter binding of proteins like HP1α or associations with other structures such as lamina (Strom et al., 2017). Therefore, the shape and form of foci are representative of complex polymer chemistry and the unique transcriptional microenvironment it forms in the nucleus.

Although a functional role for heterochromatin foci has yet to be conclusively determined, there is evidence for a range of potential functionality. One of which is differential gene expression as part of cell fate and neural differentiation. In Olfactory Sensory Neurons, each will only express one of the many thousands of olfactory receptor genes, representing sensitivity to one odor (Clowney et al., 2012). In a striking example of 3D nucleus organization, it has been shown that every non-expressed Olfactory Receptor gene will be associated with a heterochromatin foci, except for the olfactory receptor expressed by that neuron (Clowney et al., 2012). The single expressed Olfactory receptor is within the nuclear periphery, while the non-expressed OR's in heterochromatin foci are on the membrane (Clowney et al., 2012). Expressing Lamin B receptors was sufficient to terminate this organization (Clowney et al., 2012), highlighting that foci have a role in the gene regulation that drives cell identity and function, as well as the multifarious and competing mechanisms involved in foci formation.

Forming foci is an active, regulated process. It has been shown that deleting the ATP dependent proteins Setdb1/2, or all six H3 Methyltransferases, results in a major reduction in the number of chromocenters and an altered morphology (Pinheiro et al., 2012). Additionally, proteins containing a Methyl-CpG binding domain, such as MECP2 and MBD2, are concentrated at the chromocenters (Brandle et al., 2022). When these proteins are expressed in myoblast cell culture, fewer chromocenters are formed (Brero et al., 2005), and in vitro experiments have demonstrated that the Methyl-CpG Binding Domain on MECP2 can oligomerize Nucleosomes directly (Georgel et al., 2003). However, despite these observations, no “gross defects” to chromocenter formation have been detected in Loss of Function MECP2 mice (Brandle et al., 2022; Brero et al., 2005).

Of the many chromatin-associated proteins, MeCP2 has been widely studied in the context of Rett syndrome, a neurodevelopmental disorder caused by mutations in the *MECP2* gene (Rietveld et al., 2015). MeCP2 is a methyl-CpG binding protein that can directly oligomerize nucleosomes and modulate gene expression, often acting as a transcriptional repressor (Good et al., 2021). Alterations in *MECP2* dosage have been shown to significantly impact heterochromatin foci number, size, and morphology (ito-ishoda, 2020) . Importantly, in *MeCP2*^+/– female mouse models of Rett syndrome, cells exhibit a mosaic pattern due to random X-chromosome inactivation—some cells express the wild-type *MECP2* allele while others express the mutant allele (Rietveld et al., 2015). This mosaicism provides a unique opportunity to examine cell-autonomous effects of MeCP2 deficiency in neuronal circuits. In such models, disruptions in gene regulation lead to many effects, including the excitation/inhibition (E/I) ratio in neurons (Rietveld et al., 2015).

Chapter 1.5: methods to study chromatin architecture

Most efforts to study the heterochromatin structure and the “3D Genome” involve either biochemical assays or microscopy-based methods like Fluorescence In Situ Hybridization (FISH). The most common is CHiP and its high-throughput derivatives, such as Hi-C, which identify protein-DNA interactions (Gulino et al., 2021). There is also ATAC-seq, which identifies regions of the DNA with open chromatin (Dong et al., 2024).

There are some existing methods for studying the spatial organization of the nucleus using microscopy. The most notable involves FISH, which involves a DNA “probe” that complements a region of DNA of interest (Gulino et al., 2021; Won et al., 2021; Shakoori et al., 2017). FISH has been used to visualize the locations of chromosomes and other marker regions, and for comparing and contrasting the distribution of markers between cell types, including neurons, in vivo (Takei et al., 2021; Akhmanova et al., 2000). FISH has been instrumental in validating functional roles of 3D heterochromatin architecture (Aguirre-Lavin et al., 2021).

Prior studies have surveyed DNA formations using Nissi stain. From their qualitative observations, they report a general pattern of decreased amount of heterochromatin in neurons with larger nuclei (García-Cabezas et al., 2018).

Schmid et al. (2017) developed a software package for analyzing the relative compaction of heterochromatin within nuclei. Specifically they were interested in the distribution of compaction, categorizing nuclei as more evenly distributed or more extreme compaction differences. Grabowska et al. (2022) extended this method of analysis to investigate how the variance in compaction levels differ upon Long Term Potentiation to cultured neurons, and found a small but statistically significant difference after LTP induction. These methods are able to detect a rearrangement of heterochromatin, but do not detect where that arrangement occurs.

There are also methods used to morphologically characterize heterochromatin foci. At its most basic, some studies have counted the number of segmented foci per nucleus in different neuron types and under different phenotypes (Jost et al., 2015). Ito-Ishida (2020) averaged descriptors like volume and circularity for each foci in the nucleus, and attempted to resolve morphological differences based on MECP2 protein. Other authors have used similar techniques involving simplistic descriptors (Fishcher et al., 2023; Fortuny et al., 2021; Song et al., 2014) for heterochromatin formation. There are also more sophisticated 3D localization and statistical techniques available in proprietary software, but are less accessible than open sourced methods (Randall et al., 2022).

Some papers have looked at heterochromatin morphology using more complex methods. Some methods have looked at inter-foci distances, such as (Aguirre-Lavin et al., 2021; Girdhar et al., 2022), often in conjunction with FISH. Other studies have used a form of highly abstract “fingerprinting” using the SIFT algorithm, but only in 2-dimensional images (Boettiger et al., 2016), and not for experimental purposes. Increasingly sophisticated method of characterising 3D heterochromatin architecture has involved neural networks, which has been done for cultured cells.

1.6: Study Objectives

Most neurons have diffuse chromatin structure, however Purkinje neurons are an exception to this trend. These neurons possess a central “ring” structure within their nucleus (Figure 3.1). Interestingly, this can be missed at first glance as some of these neurons appear to have a central “blob”, as opposed to a ring. Only when the image stack is rotated 90 degrees is the ring structure revealed. This observation highlights what has mostly been demonstrated with biochemical assays; the nucleus has a high degree of spatial organization, and varies between neuron types (Martino et al., 2023; Girdhar et al., 2022)**.** In spite of this, few studies have surveyed 3D heterochromatin formations across neuronal cell types using microscopy.

Although chromatin often appears diffuse and nebulous, could closer examination reveal an underlying spatial organization - less like a nebula, and more akin to a constellation?

Specifically, we question how 3D Structure of Heterochromatin varies:

- Within individual neurons of the same type?
- Between individual neurons of different types?
- Between individuals of the same type, but with a single-gene mutation (Loss of Function to MECP2)?

Our approaches:

- Compare the distribution of intensity values in the nucleus, inspired by **(**Grabowska et al., 2022**)**
- Measure the count and 3D morphology of individual foci, like (Ito-Ishida et al., 2020)
- Compare the “overlap” and “positioning” of foci in nuclei that have been superimposed.

Chapter 2: Methods

2.1: Animal Care and Fixation:

Mice were housed on a 12 hour day/night cycle and fed *ad lib*. The mutated allele for LOF to MECP2 from the Mecp2tm1.1Jae/Mmcd mice (Jaenisch et al., 2004) was proliferated in C57BL/6 mice. Experimental protocols were approved by the Animal Care Committee at the University of Victoria and all experiments were performed in accordance with guidelines from the Canadian Council of Animal Care.

Adult mice were anesthetized using isoflurane gas and transcardially perfused with 4% paraformaldehyde (PFA) in phosphate-buffered saline (PBS). Following perfusion, brains were carefully removed from the skull and post-fixed overnight in 4% PFA at 4°C. After fixation, brains were rinsed in PBS to remove residual fixative and stored in PBS at 4°C until further processing.

Genotyping of mice was performed using PCR on genomic DNA extracted from ear clips, with primers targeting MECP2 alleles. Secondary confirmation of genotype was conducted by measuring the nuclear area of GFP-positive vs. GFP-negative neurons in Fiji **(**Schindelin et al., 2012). Brain weights were recorded before sectioning.

2.2 Sectioning

Brains were embedded in agar for sectioning using a vibrating microtome. The plane of sectioning varied by brain region: coronal sections were used for the cortex, striatum, and hippocampus, while sagittal sections were used for the cerebellum.

Each brain was first bisected with a coronal cut at the level of Bregma to separate anterior and posterior regions. The anterior portion, containing cortex, striatum, and hippocampus, was placed in a weight boat with the posterior face oriented down and required no additional trimming. For the posterior portion containing the cerebellum, a straight transverse cut was made on the left hand side to create a flat base. This cut surface was placed downward in the weight boat for embedding.

A 3% agarose solution was prepared in distilled water, heated in an erlenmeyer flask until fully dissolved (about 18 seconds total), and poured into a weight boat to embed the brain tissue. The tissue was positioned to ensure correct orientation for sectioning, and the agarose was placed on a level surface at 4°C to solidify.

Once solidified, the agarose block was trimmed with a razor blade to optimize stability during sectioning. For coronal sections, the block was shaped into a trapezoid with the base aligned to the ventral side of the brain. For sagittal cerebellar sections, the agarose was shaped into a ramp with a gradual incline facing away from the blade direction to reduce shear and vibration from the cutting.

Before mounting, any residual glue on the microtome stage was removed with a razor blade to ensure a level surface. A thin layer of fresh cyanoacrylate glue (Krazy Glue) was applied to the stage, and the agarose-embedded brain was positioned with the region containing the most white matter facing the blade. The vibrating microtome was set to a speed of 3 with the highest frequency setting. Sections were cut at a thickness of 75 µm. A small drop of PBS was applied to the agarose surface during sectioning.

Sections were collected using either a fine-tip paintbrush or a modified plastic eyedropper (tip removed to fit the brain section) and transferred into individual wells containing PBS for storage at 4°C. To minimize evaporation and maintain sample integrity, wells were occasionally sealed with Parafilm around the edges. Excess agarose and brain tissue was discarded according to UVic’**s** biosafety protocols.

2.3 Staining

Brain sections were stained with 4′,6-diamidino-2-phenylindole (DAPI). A staining solution was prepared by diluting DAPI (Cayman Chemical Company) to a final concentration of 20 nM in 0.1% Triton X-100 in PBS. Selected sections were incubated in the DAPI solution overnight at room temperature.

Following incubation, sections were rinsed in PBS for 1-2 hours with a minimum of three PBS exchanges. Most sections were rinsed by transferring them to adjacent PBS-filled wells; however, for more fragile tissue, such as hippocampal sections, rinsing was performed within the same well by aspirating and replacing the PBS to protect it from tearing.

2.4 Mounting

DAPI-stained sections were mounted on adhesive-coated microscope slides (75 × 25 × 1.00 mm, Newcomer Supply). A few drops of PBS were placed on each slide, and sections were transferred using either a fine paintbrush or a modified wide-mouth eyedropper (tip removed). While most sections were handled with a paintbrush, hippocampal slices were transferred using suction via the eyedropper to prevent folding or tearing.

Sections were carefully unfolded, aligned with the same dorsal-ventral orientation, and positioned close to each other but without overlap. Slides were left to air-dry until the sections became transparent and the edges appeared dry, but not wrinkled. Care was taken to avoid over-drying, as wrinkled edges indicate excessive dehydration, and can distort cell/tissue morphology.

Once dry, a drop of Immu-Mount mounting medium (Epredia) was applied to each section. The coverslip (22 × 22 x 1 mm, VWR Scientific) was gently lowered at a ~45° angle to minimize air bubble formation. Once Immu-Mount has had at least 1 day to dry, coverslips edges were sealed with nail polish to prevent desiccation during storage.

To optimize fluorescence preservation, Immu-Mount was pH-adjusted to 8.5 using sodium bicarbonate, and in some cases, trace amounts of HCl. The pH was verified using test strips (VWR Scientific) to enhance the signal of the fluorescent reporter enhanced GFP (eGFP).

Mounting was performed on a dark background to improve visibility of transparent sections. For consistency and comparative analysis, multiple regions were mounted on shared slides: F3, FN1, and FN2 cortical sections were mounted and imaged together on a single slide, as were F3, FN1, and FN2 cerebellar sections. F6 and YFP-expressing mouse cortical regions were mounted on individual slides.

Cortical Layer 1, 2 and Striatum were imaged at approximately 1.42 Bregma, Hippocampus at approximately -1.46 mm Bregma. Cerebellar sections were chosen approximately 1.4 mm from midline.

2.5 Microscopy

All imaging was performed using a Nikon C2+ laser scanning confocal microscope with a CFI Apochromat TIRF 100× oil-immersion objective lens (NA 1.49) at room temperature. Nikon Type A immersion oil (refractive index = 1.515) was used throughout. Images of cerebellar Purkinje neurons were acquired using the manually controlled Nikon Eclipse Ni-L stage, while cortical, striatal, and hippocampal sections were predominantly imaged using the motorized version of the Ni-L stage.

All image stacks were acquired using standardized parameters where possible. Each Z-stack had an XY pixel resolution of 0.04 μm and a Z step size of 0.2 μm. Most regions were imaged with both 405 nm and 488 nm lasers simultaneously (exception is hippocampus), with 2× frame averaging. Imaging parameters were occasionally adjusted between brain regions to account for differences in fluorescence intensity and tissue characteristics, to ensure accurate representation of biological signals. For hippocampal sections, only the 405 nm excitation laser was used.

Laser power was adjusted as needed to produce an average signal intensity (visually assessed) between 2000–3500 (no units). Stacks with average signal intensity below approximately 1200 (visually assessed) were excluded from analysis. Detector gain was also adjusted slightly to optimize signal without introducing saturation, with typical values ranging from 95–108 for the 405 nm channel and 100–114 for the 488 nm channel. The pinhole size was set to 30 μm for all acquisitions. Pixel dwell time was maintained at 4.8 μs. Only nuclei with minimal out-of-focus fluorescence within the nuclear boundary were selected for imaging to preserve accuracy in subsequent analysis. See the microscope parameters in Table 1.

Neuron	**Pinhole Size (µm)**	**Pixel Dwell (µs)**	**Pixel Size (XY; Z, µm)**	**Image Size (px)**	**Laser Settings**	**Stage Type**	**Z-Stack Size**
Purkinje	30	4.8	0.04; 0.2	515 × 512	Variable	Manual	Variable; Fit to nuclei size
Cortex (Layer 2/3)	30	4.8	0.04; 0.2	515 × 512	Fixed	Motorized	Fixed; extra z-height
Striatum	30	4.8	0.04; 0.2	515 × 512	Fixed	Motorized	Fixed; extra z-height
Hippocampus (CA1)	20	>4.8 (eq. Of 4.8 for 2048x2048)	0.04; 0.2	2048 × 2048	Fixed	Motorized	Fixed; extra z-height

Table 1: Imaging Settings for Different Neuron Groups

2.6 Acquisition Workflow

For cerebellar Purkinje neurons, manual acquisitions were used. For each brain slice, imaging began at a defined starting point, and fields of view (FOVs) were acquired sequentially along the folds of the cerebellum to avoid re-imaging the same region. Suitable Purkinje cell nuclei were identified at each FOV, and Z-stack bounds were manually determined to ensure complete nuclear coverage, with a slight additional “buffer” space above and below to prevent truncation. Lower laser power settings were used during preview scans to minimize photobleaching. Most Purkinje stacks were acquired near the bottom of the coverslip, where signal intensity was highest.

For cortical, striatal, and hippocampal imaging, motorized acquisition was employed using the Multi-Point acquisition feature on Nikon NIS-Elements AR software. Points of interest were selected based on a preview scan, with each Z-stack centered around the midplane of the nucleus. Consistent Z-depth margins were included to avoid cutting off nuclear boundaries.

Hippocampal neurons were imaged with a larger scan area (2048 × 2048 pixels). Image stacks from this region were later cropped into sub-stacks containing individual nuclei, which were then processed identically to stacks from other brain regions. All hippocampal neurons were selected from the CA1 region, which was anatomically identified using the Allen Brain Atlas.

Layer 2 cortical neurons were imaged starting from the medial cortex and proceeding laterally across the brain section to ensure spatial sampling consistency.

2.7 Image Processing

All image analysis was performed using Fiji (v1.54f) and custom Python scripts developed and run in an Anaconda 24.5.0 environment using the Spyder IDE (v5.4.3). Analysis was conducted on a Windows 10 Enterprise system equipped with an Intel(R) Core(TM) i7-7700K CPU (4.20 GHz) and 16.0 GB of RAM. A modular pipeline was implemented following a "Separation of Concerns" principle, with distinct modules for thresholding, manual despeckling, foci quantification, similarity metrics, and visualization/statistical analysis.

Image stacks were first split into individual channels (DAPI and GFP) and saved in TIFF or TIF format. Each stack was manually cropped in Fiji to isolate individual nuclei from the background and neighboring cells. The bounds of the nucleus are defined by the DAPI channel.

Image stacks were converted to 8-bit format (Fiji) prior to thresholding. Multi-Otsu thresholding (Scikit-Image, v0.23.2) was applied independently to each image stack using 6 discrete classes. This number was chosen as a compromise between segmentation granularity and algorithmic time-complexity: stacks required ~3 minutes to process with 6 classes, whereas 7-class thresholding significantly increased processing time to multiple hours per stack. The Pixel Count and Coefficient of Variation was saved for each image stack thresholded.

Each image stack required an average processing time of approximately 9.1 minutes after binarizing. Following thresholding, image stacks were binarized by selecting the threshold class that best corresponded to heterochromatin condensates. This class was chosen through manual inspection by an unblinded operator. A median filter (radius = 1) was applied to reduce noise. The morphological operations binary “open” and “close” (Fiji) were then applied to refine object boundaries. Remaining speckles or artifacts were manually removed using Fiji’s paint tool.

Intermediate outputs - cropped images, multi-thresholded stacks, and final binary masks - were saved for quality control and downstream validation.

Final binary image stacks were analyzed using *Geometric Foci Measurements* and the *Degree of Similarity* metric (see Supplemental Methods). This metric was applied to assess spatial organization of nuclear features across different brain regions.

Nuclei exhibiting substantial out-of-focus fluorescence or overlapping with neighboring cells were excluded from analysis. Additionally, as defined in the *Validation* (Supplemental) section, any nucleus exhibiting a rotation greater than 60° (geodesic distance) was excluded. All data and source code are stored locally on the primary workstation in Kerry’s laboratory.

2.8 Morphological Measurements

Morphological measurements were performed using custom Python scripts developed in Spyder (v5.4.3) and executed in an Anaconda 24.5.0 environment. Image stacks were first processed into binary masks as described in the Image Processing section. These masks were loaded as 3D NumPy arrays, and voxel dimensions were defined based on confocal imaging parameters: 0.037 µm in XY and 0.2 µm in Z. Due to anisotropic voxel dimensions, Z-planes were linearly interpolated (scipy.ndimage.zoom) to match the XY resolution, creating isotropic stacks for accurate 3D shape analysis.

Each interpolated binary mask was converted into a point cloud by extracting all non-zero voxel coordinates. Connected components were identified using a 26-connectivity structure element. Components smaller than a predefined volume threshold (200 voxels) were excluded from downstream analysis. For each retained object, geometric properties were computed. Volume was calculated as the number of voxels in the component, scaled by voxel area in microns^2 (XY-plane only).

Principal axis lengths and shape features were computed by applying eigenvalue decomposition to the 3D coordinate covariance matrix of each object. The lengths of the major, intermediate, and minor axes were defined as 4× the square roots of the sorted eigenvalues. Shape distortion was quantified using ratios of the axis (major-to-minor) and ellipticity, defined as:

Ellipticity = 1 − Minor Axis Length / Major Axis Length

Centroid coordinates and bounding box dimensions (in voxels) were also computed for each object. All metrics were stored in a Pandas DataFrame and averaged across all detected components (foci) within each nucleus. Only nuclei with one or more components above the volume threshold were kept in the final dataset. Results were exported as .csv files for statistical analysis.

2.9 Data Analysis

All plots were made in Seaborn and statistics were made with SciPy. For plots with jitter, values had +/- a jitter value drawn from a uniform distribution (Numpy Random). To estimate confidence bands for the cumulative histograms), I applied a bootstrap resampling by repeatedly sampling with replacement from the original data (Uniform Distribution from Numpy's Random module). The 2.5th and 97.5th percentiles of these bootstrap CDFs at each grid point were then used to construct a 95% confidence band around the original KDE-based CDF. Counts of GFP POS vs. NEG nuclei were recorded.

Software Versions: Numpy: 1.26.4, SciPy: 1.11.4, Sklearn: 1.2.2, Skimage: 0.23.2, Open3D: 0.18.0, Blender: 4.3, Seaborn: 0.12.2, Matplotlib: 3.8.0, Pandas: 2.1.4, Python: 3.11.7, Tiffle: 2022.10.10, Spyder: 5.4.3, Fiji: v1.54f, scikit_posthocs: 0.11.4.

Chapter 3: Results

The initial observation that motivated this study was observing that Purkinje neurons had remarkably consistent chromatin structures (Fig 3.1). In the cerebellum, with only DAPI stain, every Purkinje nuclei we observed had the same ring-like chromatin structure. There were a few “blob”-like chromatin spheres, but upon viewing them from the side in an image stack, it was clear that these were rings as well, just oriented vertically. Chromatin from numerous neuron types of the brain were imaged and displayed in Figure 3.1. This non-random organization led to questions of how consistent the chromatin is in other kinds of neurons, especially those with seemingly random foci positioning.

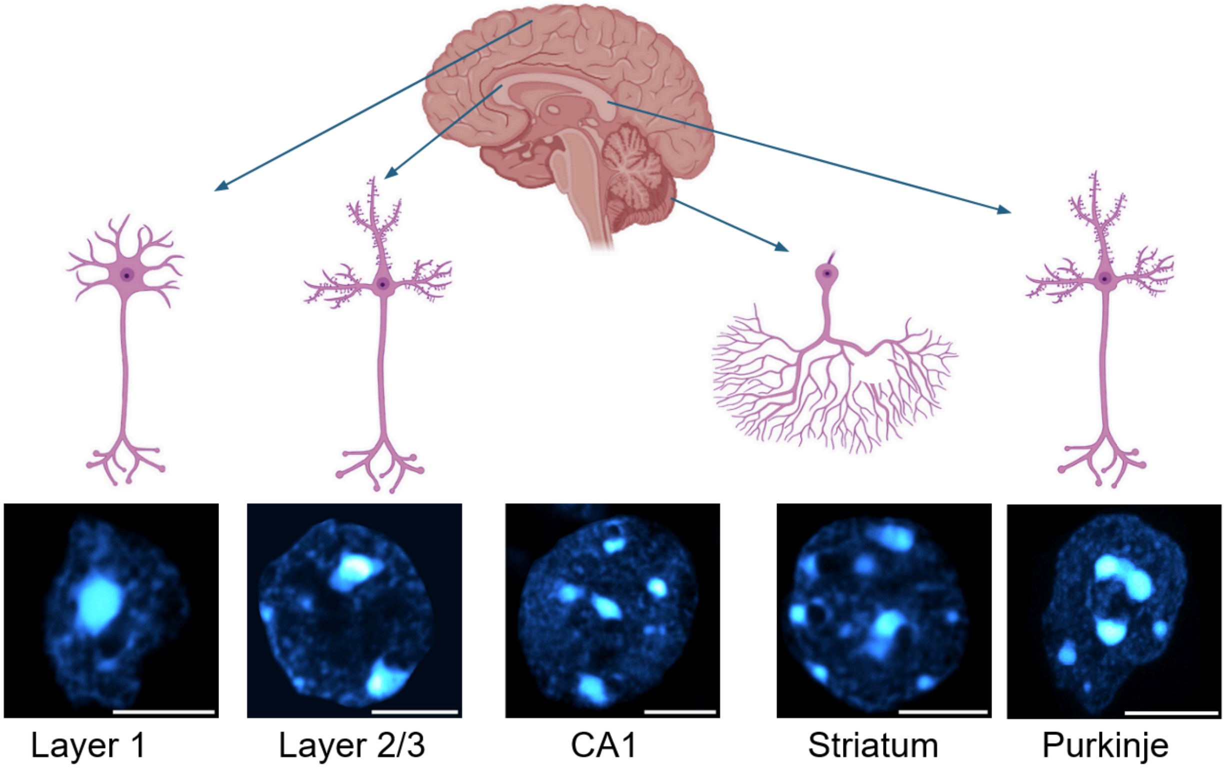

Figure 1: Qualitative Observations of Chromatin Architecture Across the Brain
A) Schematic of a (human) brain showing sampled regions and cartoon depictions of neurons with varying morphological features.
B) Representative DAPI-stained nuclei from Purkinje, cortical, striatal, and hippocampal neurons. Purkinje neurons show a ring-like chromatin structure, while others exhibit more heterogeneous foci. All scale bars are 10 micron. Representative images were processed with a 1-pixel median filter (Fiji).

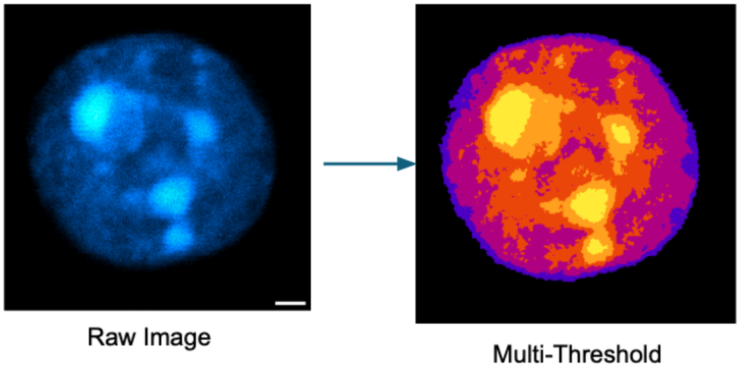

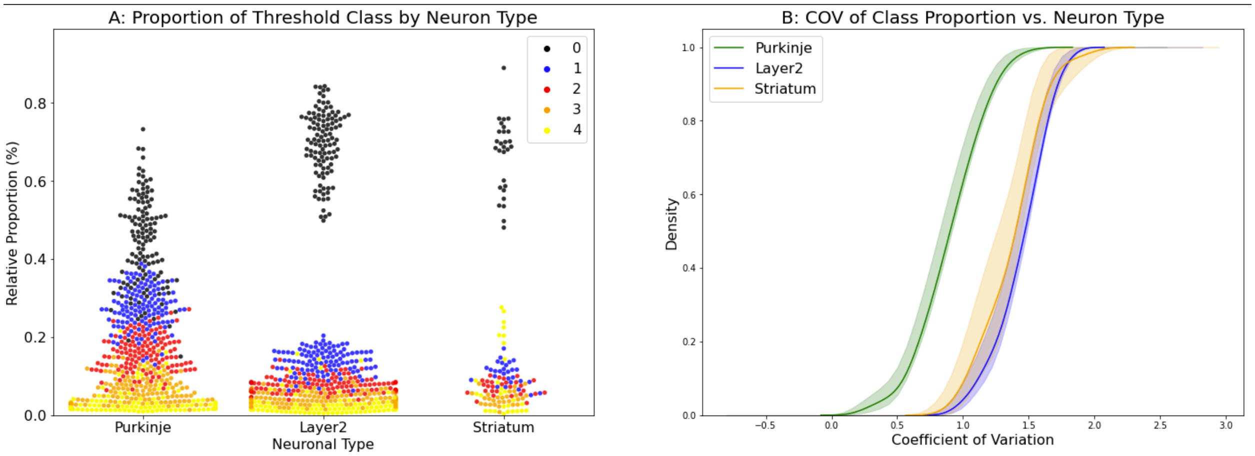

Figure 2. Multi-Otsu Thresholding Differentiates Neuronal Chromatin Organization. Intensity segmentation and class-based voxel analysis were performed following the method of Grabowska et al. (2022).
(A) Proportion of chromatin voxel intensity classes across neuronal types, determined via multi-Otsu thresholding. Each nucleus was segmented into five discrete intensity classes (0–4), with each point representing the proportion of a class within a single nucleus. Purkinje neurons exhibit a more evenly graded distribution of voxel intensities, whereas Layer 2 and Striatal neurons show higher proportions in the lowest intensity class (Class 0), suggesting increased background or less compacted chromatin.
(B) Cumulative density function (CDF) of the coefficient of variation (COV) of class proportions across neuronal types. Purkinje neurons show lower COV, indicating more consistent chromatin compartmentalization. In contrast, Layer 2 and Striatal neurons exhibit greater variability. Shaded regions indicate 95% bootstrapped confidence intervals (n = 10,000).

Following Grabowska et al. (2022), we applied multi-Otsu thresholding on image stacks of DAPI stained nuclei, which divided the intensity values into 5 discrete bins. The variance in the relative proportion of each threshold class differed between brain regions. Purkinje neurons had a lower coefficient of variation, and a more graded proportion of intensity classes. In comparison, a larger proportion of Hippocampus and Layer2 voxels were assigned to the background threshold class. The high intensity threshold class was binarized and used for subsequent measurements.

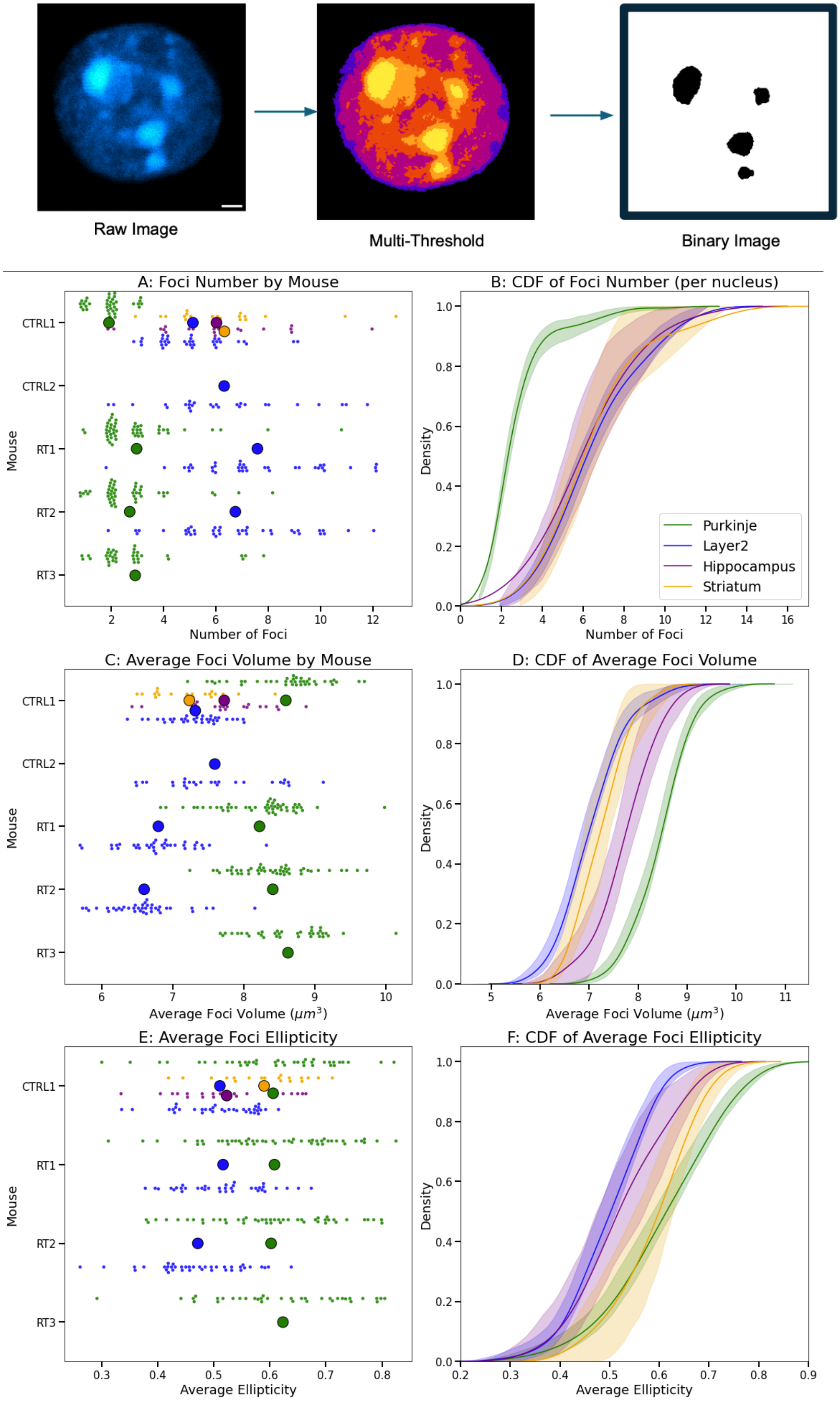

Figure 3. Morphological Properties of Heterochromatin Foci Vary Across Neuronal Types and Individual Mice. All morphological metrics were derived from 3D reconstructions based on methods adapted from Ito-Ishida et al. (2020).

(A) Number of 3D heterochromatin foci per nucleus across individual mice and neuronal types. Each dot represents a nucleus; color indicates neuronal type. Jitter was applied for clarity. Purkinje neurons exhibit distinctly higher foci counts, particularly evident in RT3.
(B) Cumulative density function (CDF) of foci number per nucleus, stratified by neuronal type. Purkinje neurons show consistently higher foci counts, while Layer 2 neurons have the fewest.
(C) Average foci volume per nucleus across mice. Purkinje neurons show higher average volumes.
(D) CDF of average foci volume per nucleus by neuronal type. Purkinje neurons exhibit significantly larger foci volumes compared to other types.
(E) Average foci ellipticity per nucleus. Ellipticity is defined as 1−(major axis /minor axis), higher values indicate more elongated foci.
(F) CDF of average foci ellipticity by neuronal type. Purkinje neurons show higher ellipticity values, though the separation is more subtle than for volume or number.

We measured the number, volume, and ellipticity of heterochromatin foci using 3D geometric measurements that were recreated from Ito-Ishida et al. (2020). The average foci volume varied across neuronal types: Layer 2 had a mean volume of 6.9 μm^3 (SD = 0.69 μm^3, n = 170), CA1 (Hippocampus) had 7.49 (SD = 0.60 μm^3, n = 21), and Striatum had 7.00 μm^3 (SD = 0.513, n = 20).

Statistical tests for differences in Volume, Ellipticity, and Number of Foci between neuron types were made with Kruskal-Wallis followed by Dunn’s Post Hoc Test. This was done because Shapiro-Wilk and Levene’s Tests revealed that the assumptions of equal variance and normality were not met. The P-values from Dunn’s Post Hoc tests were corrected with Bonferroni. Kruskal-Wallis revealed that foci volume was significantly different between neuron types (H = 198.18, p=1.042^10-42). Purkinje neurons had significantly larger foci volumes compared to CA1/Hippocampus (p = 0.0023), Layer 2 (p < 1.0 × 10^-42), and Striatum (p = 3.94 x 10^-8). No significant volume difference was found between CA1 and Striatum (p = 0.394). In terms of Ellipticity, Kruskal-Wallis revealed differences between neuronal groups (H= 8.496, p=3.67 x 10^-02). The only neuron group significantly different was Purkinjes with Hippocampus (p = 0.021). For the number of foci, Kruskal Wallis revealed significant differences between groups (H=629.07, p = 1.33 x 10-131).

To further characterize neuronal heterochromatin foci, we aimed to move beyond summary descriptors, and directly compare the conformation of heterochromatin between nuclei. To answer this question, we developed two spatial metrics: the *Degree of Morphological Similarity* metric and the *Degree of Spatial Similarity* metric.

Figure 4.C shows the process of this assay. Briefly, both of the *Similarity* assays convert Image Stacks into 3D objects (“Point Clouds”). By superimposing all of the foci (*Degree of Morphological Similarity*) between two nuclei, we obtained a value analogous to “overlap”. However, we also wanted to directly measure the positioning of foci in a morphology agnostic manner. To do this we found the superimposed center point of each foci (*Degree of Spatial Similarity*).

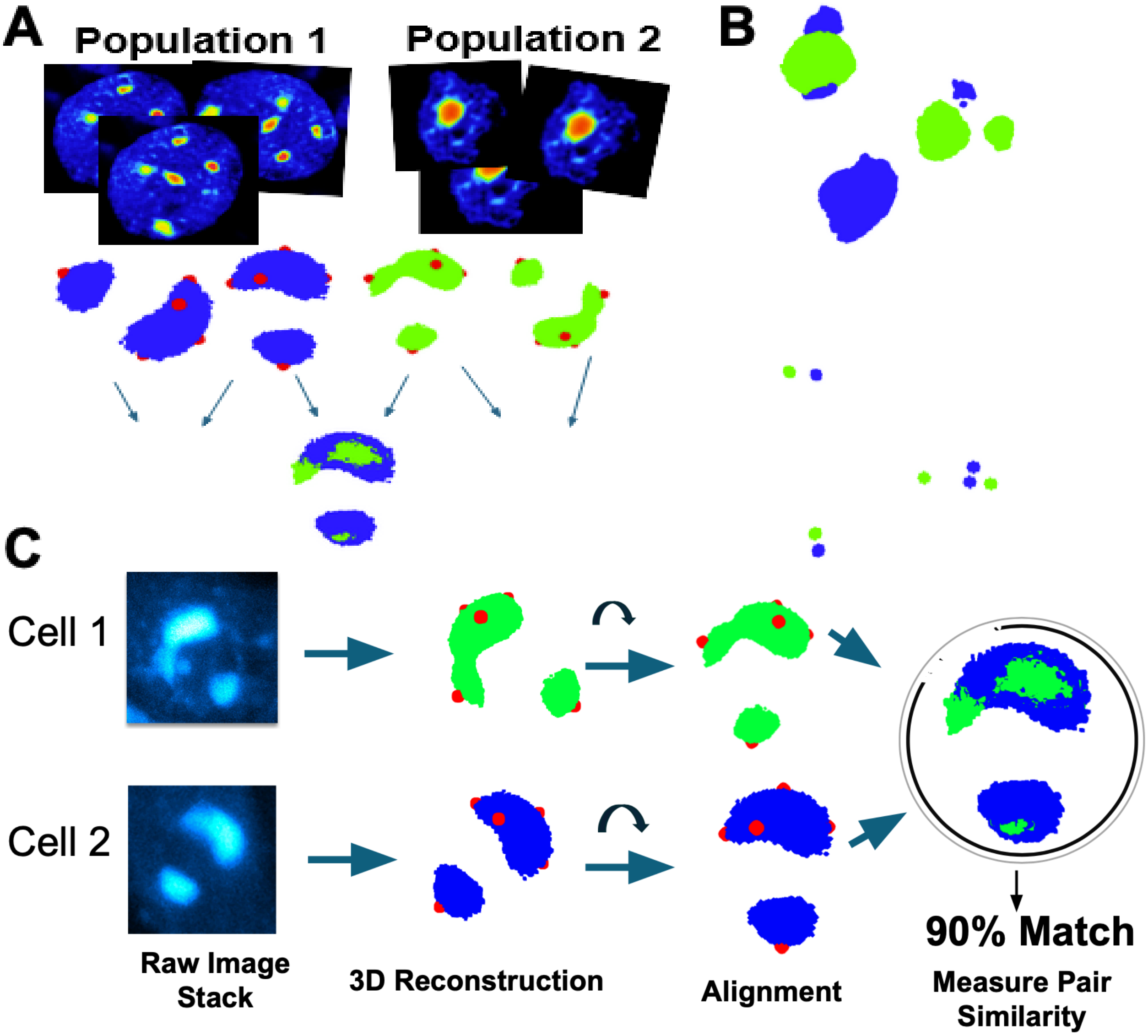

Figure 4: Overview of the *Degree of Similarity* Metrics.
A) Flow chart showing the pipeline of converting a raw image stack into a 3D Point Cloud, aligning it to a common orientation, and measuring the Similarity. Similarity is the Root Mean Square distance of each coordinate to its nearest neighbor.
B) Comparison of foci as measured in *Degree of Morphological Similarity*, and their centroids (bottom), which are measured in *Degree of Spatial Similarity*. Centroids are enlarged for demonstration.
C) Diagram explaining how populations of neurons, in this case within-group (Purkinje-Purkinje) comparisons, are made pairwise in all possible combinations. C) How the Degree of Similarity metric was applied to populations of same or different neuronal types in a pairwise manner.\

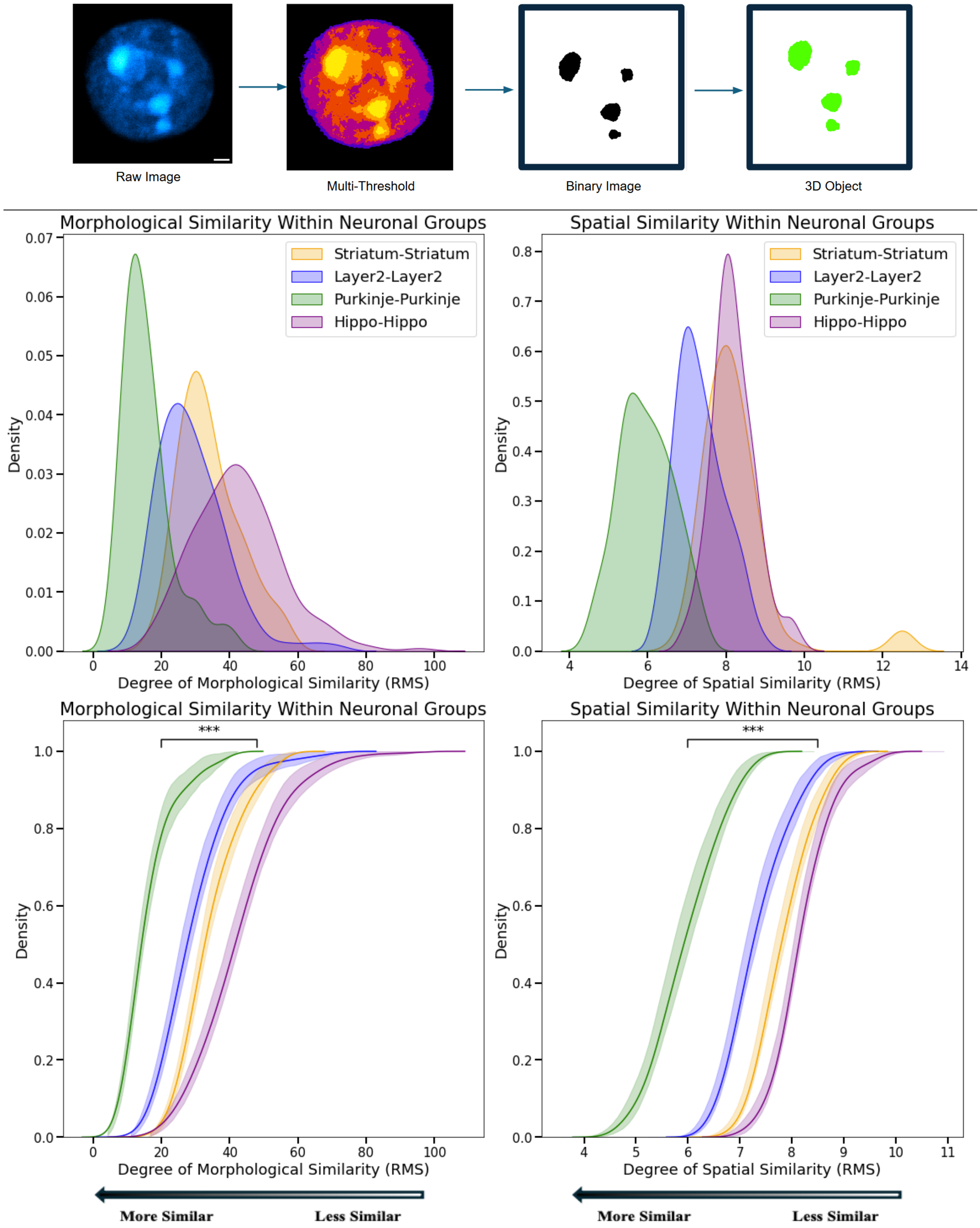

Figure 5. Neuronal Groups Can be Distinguished by *Degree of Similarity*

(A) Kernel density estimates of pairwise morphological similarity (based on foci shape/volume

overlap) among nuclei within each neuronal type. Purkinje–Purkinje pairs showed the highest similarity (lower RMS values), followed by Layer 2, Striatum, and Hippocampus.
(B) Cumulative distribution of morphological similarity scores. Purkinje neurons demonstrated significantly higher within-group similarity compared to Layer 2 neurons (Bonferroni Corrected Dunn Post Hoc P = 1.92 x 10^-13).
(C) Kernel density estimates of pairwise spatial similarity (based on relative foci positioning) among neurons of the same type. Purkinje neurons showed the greatest internal consistency.
(D) Cumulative distribution of spatial similarity scores mirrors the morphological trend, with significant separation between Purkinje and Layer 2 groups (Bonferroni Corrected Dunn Post Hoc P = 1.92 x 10^-13).

To measure population-wide similarity in terms of foci “overlap” and “positioning” amongst neurons of the same type, we performed within-group comparisons using the *Similarity* metrics described in Figure 4. These assays yield a numeric readout for a pair of nuclei at a time. We applied to all possible pairs of nuclei within matching neuronal populations. Every pairwise measurement was made into a histogram (Figure 5).

The *Degree of Spatial Similarity* showed that Purkinje-Purkinje pairs was the most *Similar* within-group comparisons(mean = 5.95, std = 0.678), less for Layer2–Layer2 (mean = 7.33, std = 0.61), and moderate for other pairings, including Striatum–Striatum (mean = 7.84, std = 0.55) and Hippocampus-Hippocampus (mean = 8.18, std = 0.55). Kruskal-Wallis indicated a significant difference amongst all comparison types (including within and between groups)(H=629, p=1.33 x 10^-131).

After assessing within-group similarity, we next evaluated *Degree of Spatial Similarity* between neuron types (Figure 6). Neuronal populations were pooled, and the metrics were applied to all pairwise combinations of nuclei. Results are summarized in Figure 6, where colored lines represent within group comparisons, and black lines indicate between group comparisons. Hippocampus–Striatum had mean of 8.16 and standard deviation of 0.58 (p= 0.57). These values were intermediate, falling between the within-group values of Striatum and Hippocampus. In contrast, Hippocampus–Layer 2 showed a higher mean similarity of 8.54 and standard deviation of 0.61 when compared to hippocampus-hippocampus within-group similarity (p = 0.00147) and layer2-layer2 (6.12 x 10^-68).

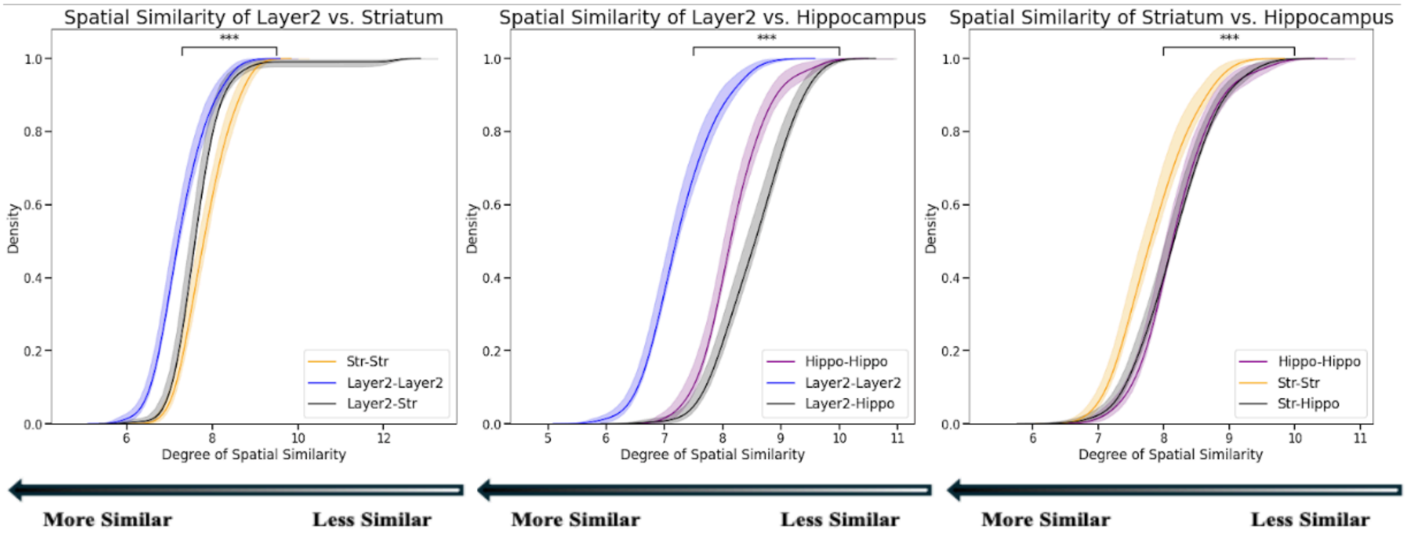

Figure 6: Similarity Between Neuron Groups. Kernel density estimates of Spatial *Similarity* scores are shown for within-region (colored lines) and between-region (black lines) neuron comparisons across three brain areas: Layer 2 (Layer2), Striatum (Str), and Hippocampus (Hippo).

(A) Spatial similarity between Layer2 and Striatum shows that the between-group distribution (Layer2–Str) falls between the within-group distributions (Layer2–Layer2 and Str–Str), indicating intermediate similarity. Significance bars show the difference between Layer2–Layer2 and Striatum–Striatum.

(B) Layer2 and Hippocampus exhibit significantly lower between-group similarity compared to their respective within-group distributions. Significance bars show the difference between Layer2–Layer2 and Hippocampus–Hippocampus.

(C) Striatum and Hippocampus show a strong separation between within-group and between-group similarities, with the lowest between-group similarity across all comparisons. Significance bars show the difference between Layer2–Layer2 and Hippocampus–Hippocampus.

Asterisks denote statistically significant differences among within-group distributions. Overall, within-region neuron groups are more spatially *Similar* to each other than to neurons from other regions.

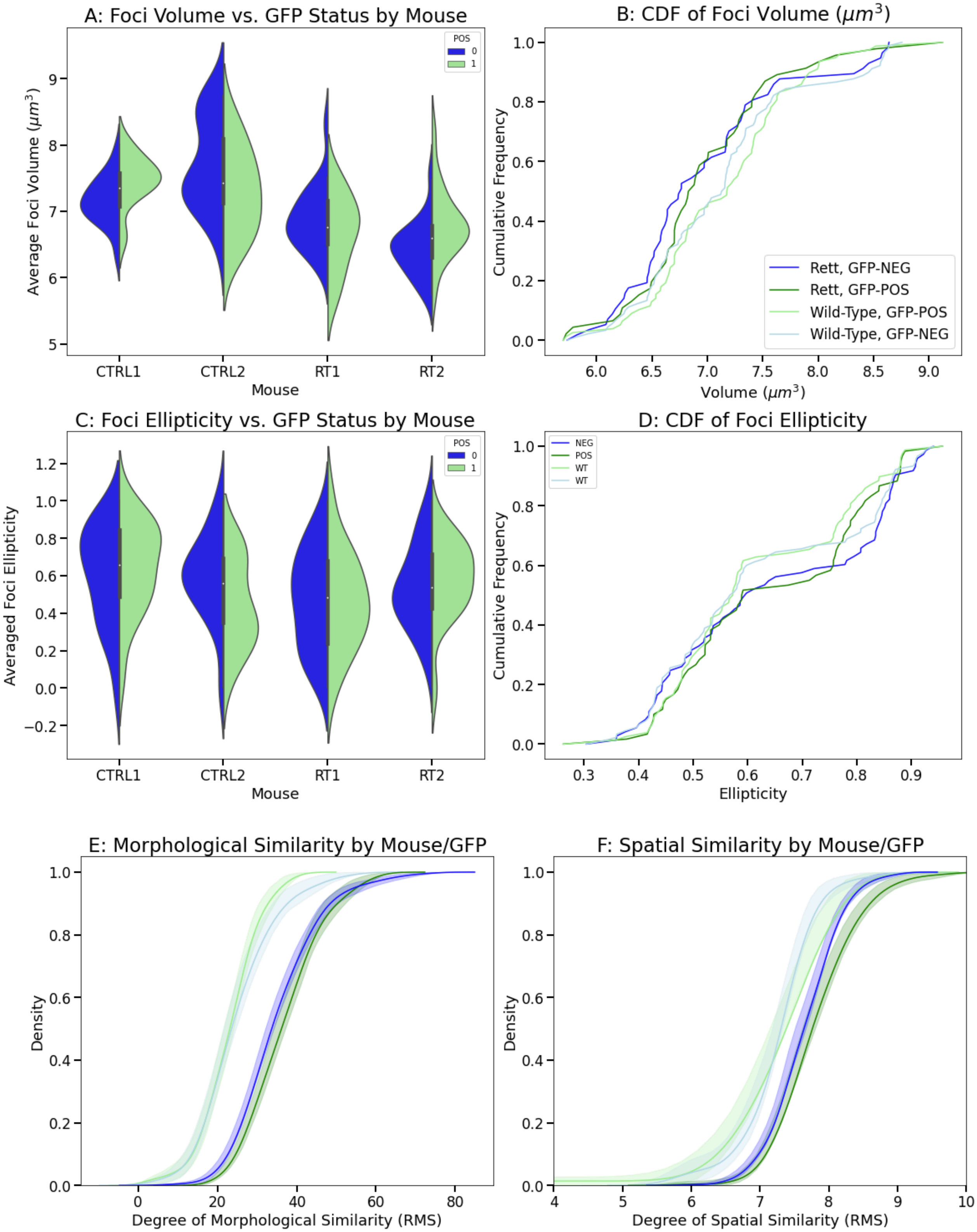
A: Foci Volume vs. GFP Status by Mouse

B: CDF of Foci Volume (μm^3)

C: Foci Ellipticity vs. GFP Status by Mouse

D: CDF of Foci Ellipticity

E: Morphological Similarity by Mouse/GFP

F: Spatial Similarity by Mouse/GFP

Figure 7. Genotype-Specific Alterations in Cortical Layer 2/3 Neuronal Chromatin Foci. Mecp2 loss-of-function (LOF) nuclei are identified by lack of GFP in the Rett mice. Statistical comparisons are reported in Table 2.
(A) Split-violin plots showing average foci volume (μm³) for GFP-positive (GFP^+) and GFP-negative (GFP^-) nuclei across individual mice. Wild-type (WT) controls (CTRL1, CTRL2) are shown on the left; Rett syndrome (RTT) mice (RT1, RT2), including the Mecp2 LOF mouse, are shown on the right.
(B) Cumulative distribution functions (CDFs) of foci volume for the groups shown in (A), stratified by genotype and GFP status.
(C) Split-violin plots of average foci ellipticity by mouse and GFP status.
(D) CDFs corresponding to the ellipticity data in (C).
(E) Distributions of morphological similarity (root-mean-square, RMS) between nuclei, with lower RMS values indicating greater similarity.
(F) Distributions of spatial similarity between nuclei, quantified by RMS differences in spatial organization; lower values indicate greater spatial similarity.

To investigate how MECP2 dysfunction influences chromatin architecture we quantified multiple structural metrics of heterochromatin foci, as seen in prior figures, including nuclear volume, ellipticity, morphological similarity, and spatial distribution. Analyses were performed using both groupwise statistical comparisons and linear mixed-effects models.

Mouse Models

We asked if foci volume is described by GFP presence, mouse genotype, and/or an interaction of the two using a linear mixed-effects model (Scipy). GFP label, Genotype were the fixed effects and the random intercept for individual mice. The model specification was: volume ~ label * genotype + (1 | Mouse).

The foci of WT mice are significantly larger than the Rett mice(b = 0.786, $p < 0.0001$). GFP pos nuclei in all mice were slightly larger (0.103, p = 0.406), and this effect was slightly diminished in Wild Type mice (b = -0.136, p=0.452). The group variance is 0.013 and the residuals is 0.284, thus most of the variation is between cells, not genotypes or individual mice. A similar analysis was done for ellipticity, and yielded no significant differences between genotype (b = 0.181, p =0.253), GFP group (b = 0.006, p =0.706), or an interaction (b = -0.016, p = 0.516).

Morphological and Spatial Organization of Heterochromatin Foci

We evaluated how GFP status and genotype influence the structural organization of heterochromatin foci by measuring *Morphological Similarity* and *Spatial Similarity*.

The model revealed a significant main effect of genotype, with WT mice exhibiting significantly lower morphological distances compared to Rett mice ($b = -10.366$, $p < 0.001$). GFP-positive nuclei showed a slight but significant increase in *Morphological Similarity* relative to GFP-negative nuclei across genotypes ($b = 1.744$, $p = 0.026$). A significant interaction was observed between genotype and GFP label ($b = -3.488$, $p = 0.013$). Group-level variance was low (1.310).

Spatial Similarity followed a similar pattern. Wild type nuclei had smaller distances, more *Spatial Similarity*, that was significantly different compared to Rett mice ($b = -0.390$, $p < 0.021$). GFP pos nuclei were larger than GFP neg nuclei across all mice ($b = 0.165$, $p = 0.002$), without a significant interaction between GFP pos and Wild Type mice ($b = -0.70$, $p = 0.075$).

In addition to cortical neurons, there is comparable data for Purkinje neurons from Control and Rett mice (Supplemental Fig. 1).

Chapter 4: Discussion

This study builds upon a growing literature that heterochromatin is not passively organized but tightly organized in neuronal nuclei. By using repurposed analytical tools, as well as introducing a 3D spatial metric, we provide a variety of demonstrations for how chromatin morphology can be quantitatively assessed in intact tissue. The methods developed in this study establish a framework for systematically assessing chromatin structure using light microscopy. We show that chromatin morphology, particularly heterochromatin organization, can exhibit non-random morphology that varies by cell-type. In this section, I will discuss the key geometric measurement results, then the *Degree of Similarity* comparisons within and between neuron types. I will conclude by zooming in and discuss the genotype specific analysis of these measurements.

4.1 Heterochromatin-to-Euchromatin Ratio

We quantified nuclear heterochromatin by computing the ratio of high- to low-intensity chromatin using a multi-Otsu thresholding approach adapted from Grabowska et al. (2022). Unlike their cultured neuron data, we applied the method to intact brain tissue and to a variety of neuronal types. Purkinje neurons showed a more consistent ratio compared to cortical layer 2/3, Striatum, and hippocampal CA1 neurons. This pattern allowed us to distinguish Purkinje neurons based on the distribution of intensities from DAPI alone. Since we cannot tell if the intermediate intensity values are euchromatin, and not background noise or out-of-focus fluorescence, our biological interpretation is limited. However, other literature sources have described Purkinje neurons overall decondensed chromatin despite the large focus (Baltanas et al., 2011).

The authors of this study assessed the proportion of nuclear volume occupied by different chromatin compaction levels after LTP in cultured neurons. They interpreted the COV of pixel proportion between thresholds as an indication of differing chromatin compaction states. Unlike Grabowska and colleagues (2022) who used cultured neurons, our study applied this method to *in vivo* tissue sections and of neurons that were of markedly different types.

Future live cell imaging studies should investigate neuron types with comparable nuclear arrangements as Purkinje neurons, such as Retinal Ganglion cells and Betz projection neurons. Under live cell imaging conditions, you can see how the distribution of intensities changes over time, which would reflect differences in euchromatin/heterochromatin compaction. Overall, our result demonstrates that intensity-based proxies of heterochromatin-to-euchromatin ratios can effectively distinguish neuronal subtypes by nuclear chromatin organization. It's also worth noting that they used more thresholding classes so it's possible they could have achieved higher granularity and sensitivity in intermediate chromatin levels and the boundaries of heterochromatin (Grabowska et al., 2022).

4.2 Geometric Measurements of Heterochromatin Foci across Neuronal Types

Quantitative analysis of heterochromatin foci revealed that, among the neuronal types examined, Purkinje neurons consistently exhibited fewer foci compared to cortical and striatal neurons. This result aligns with our qualitative observations (Fig 4.1) and prior studies that Purkinje cell nuclei tend to contain fewer but larger heterochromatin chromocenters (Wilczynski et al., 2013; Baltanas et al., 2011). Outside of Purkinje neurons, we observed high variation within neuron groups, but relatively little variation in foci number between other cell types.

4.2.1 Number of Foci

It is worth noting that the number of nuclear foci has been correlated with neuronal function. For instance, NMDA receptor-mediated stimulation can increase nucleolar number and alter nuclear architecture, which in turn affects protein synthesis and transcriptional output (Jordan et al., 2007). These results raise the possibility that activity-dependent regulation of chromatin structure may contribute to variability in foci number. Future studies correlating neuronal activity and foci count would be informative.

Although all mice in this study were adults (>P30), prior work shows that heterochromatin organization changes significantly during postnatal development. In Purkinje neurons, chromocenter number decreases from about eight at birth to five by the end of the first postnatal week (Wilczynski et al., 2013), coinciding with increased transcription and synaptogenesis. While we did not examine different developmental stages, the low number of foci in adult Purkinje neurons is consistent with this trend.

4.2.2 Volume

We measured the heterochromatin foci in Purkinje neurons to be much larger compared to other neuron types. It is curious that this observation occurred in neurons where tetraploidy - multiple copies of the genome - is thought to occur. Tetraploidy in Purkinje neurons has been described in rats (Monte, 2006), and similar polyploidy has been reported in large cortical projection neurons such as Betz cells (Nandakumar et al., 2023; Sigl-Glöckner et al., 2017). It is possible that the enlarged foci volume in Purkinje neurons is a reflection of increased genomic content. This question could be addressed in future studies using immunohistochemistry for telomeres, indicating the number of repeat sequences. It would also be interesting to analyze the heterochromatin foci of other candidate polyploid cells, such as Betz and retinal ganglion cells.

Interestingly, hippocampal interneurons - both in culture and in vivo - exhibit denser and larger chromatin foci following long-term potentiation (LTP) (Grabowska et al., 2022). These changes in chromatin condensation appear to be energy-dependent and require calcium signaling, with HDAC1 playing a mediating role (Grabowska et al., 2022).

4.2.3 Ellipticity

Our results show that ellipticity of foci differs between types of neurons. Ellipticity is an approximation of how similar an object is to a sphere, where a perfect sphere would have a value of 0.

A more spherical foci may indicate different biochemical properties and physical state that impacts transcription. Importantly, chromatin formation can be modeled as a liquid-liquid phase separation, which appears as liquid droplets through weak interactions with proteins or other nucleic acids (Guthmann et al., 2019). The rapid, spontaneous transformation and co-existence between dense and dilute phase has potential physical properties in nuclei: ability to fuse or fission, and dynamically exchange components. Heterochromatin protein 1 (HP1)-rich domains can phase-separate into liquid droplets, which tend to round up into spheres to minimize surface tension (Guthmann et al., 2019; Zhang et. al, 2023). Importantly the liquid-like nature has been proposed to explain their spherical formation to reduce surface tension (Boeynaems et al., 2018). If there are disruptions to ellipticity, this could suggest an external factor is disrupting the shape that would form spontaneously, potentially reflecting active regulation, and it is implicated in inability of chromocenters to fuse (Brangwynne et al., 2011). Furthermore, loss of circularity is associated by the inclusion of a significant amount of DNA and is possibly regulated by external structures such as lamina (Strom et al., 2018).

4.3 Degree of Similarity: Non-Random, Yet Non-Distinct

To quantify the spatial organization of heterochromatin in neurons, we developed and validated a point-set-based "Degree of Similarity" metric. This metric leverages root-mean-square (RMS) distances between aligned 3D foci configurations, offering a comparison of constellation-like foci positioning. Each comparison is done for a pair of nuclei, so a population of samples were paired in all possible combinations and the histogram of these comparisons was analyzed. We separately determined the similarity for whole foci, as well as the centroids of each individual foci. Unlike traditional approaches that assay heterochromatin foci size and/or shape, our method captures the overall spatial pattern of foci arrangement across cells, providing a more holistic measure of nuclear organization.

4.3.1 Morphology vs. Spatial Similarity Within Neuronal Types

Purkinje neurons, unsurprisingly from our qualitative observations, demonstrated a distinct morphologically similar heterochromatin arrangement. The high similarity within Purkinje cells, and their clear distinction from other neuronal types, could potentially reflect their unique development and transcriptional environment. Prior work has shown that Purkinje neurons undergo a highly stereotyped chromocenter migration during early development (P6–P21), coinciding with maximal synaptic formation and activity (Takizawa et al., 2008). By P29, kinetochore and chromocenter positioning becomes centralized and stable, supporting long-term functional maturity (Takizawa et al., 2008).

In contrast, neurons from other brain regions (CA1, Striatum, and Layer 2/3) had variable Degree of Morphological Similarity, but much less variability in centroid-based *Spatial Similarity*. The fact that morphological similarity does not differentiate as well suggests the individual foci are in different conformations but similar locations. It also highlights the potential utility of combining morphological information together.

4.3.2 Cortical and Hippocampal neurons have variable morphological/spatial similarity.

When *Similarity* is calculated between neuron types, spatial heterogeneity has modest differences compared to within-group comparisons. For Layer2-Striatum, and Striatum-Hippocampus, the distance between these groups is intermediate between the respective within-group distances. In practical terms, this means that a given Layer2 neuron is about as *Similar* to another layer 2 neuron as it is to another striatum neuron. But, the Layer2-Hippocampus group displayed a modest increase in distance compared to its within-group comparisons. This is interpreted as meaning that Layer2 neurons are less similar to a hippocampal neuron as it is to another Layer2 neuron.

The variability observed could reflect the heterogeneity of cortical neuron populations. Layer 2/3 contains multiple neuronal subtypes, including the morphologically distinct pyramidal and stellate cells, as well as variation within those classes. Prior transcriptomic and connectomic studies have noted substantial functional and molecular diversity among cortical neurons (Clowney et al., 2012). For example, the expression of glutamate receptor subunits such as NR1 and NR2B–encoded on separate chromosomes–varies significantly from neuron to neuron (Bharadwaj et al., 2014), and requires spatial interactions of chromatin to facilitate their differential transcription. Notably, disruptions in the expression/ regulation of these subunits have been linked to neurodevelopmental disorders, including autism and schizophrenia, underscoring the importance of precise chromatin control (Bharadwaj et al., 2014). Investigations into epilepsy have revealed that the spatial distribution of foci containing satellite DNA is altered, and go so far as to suggest that this “epigenetic memory” dictates repeat epileptic events. Miguel Ángel García-Cabezas et al. (2018) argue that dendritic spine morphology and neurotransmitter profiles alone are insufficient predictors of chromatin organization, and is instead reflective of the metabolic requirements to maintain large projecting axons of some neurons.

In contrast, the observed morphological variability in CA1 neurons is consistent with CA1 subtype variability. Cembrowski et al. (2016) demonstrated that neuron types found within CA1 can be as diverse from each other, as they are compared to CA3 populations, challenging the assumption of CA1 homogeneity. This "multifarious continuum of cells" likely contributes to the modest separation observed within our Spatial Similarity metric. Moreover, McKiernan et al.. (2017) reported subtype variation within CA1 neurons. Given the role of CA1 in learning and memory, responses to varying environmental demands may require a more dynamic epigenetic landscape. Indeed, environmental stimuli and neural activity are known to induce chromatin remodeling in hippocampal neurons, including spatial reorganization of satellite DNA during long-term potentiation (Vadakkan et al., 2006). Similarly, Das et al. (2023) noted changes in nuclear morphology - such as reduced circularity - associated with increased transcriptional activity in neurons.

4.3.3 Summary of Within Neuronal Types

In conclusion, by comparing individual neuron classes, such as CA1 pyramidal neurons, striatal neurons, and layer 2/3 cortical neurons, the Spatial Similarity metric was sufficient to distinguish populations of neuron types to a statistically significant degree. However, the effect size was modest, suggesting that while there is structure to the spatial arrangement, it is not rigidly stereotyped like Purkinje neurons are.

4.3 Genotype-Specific Effects

The use of a mosaic MECP2 loss-of-function (LOF) model allowed us to directly compare chromatin architecture between MECP2-expressing and MECP2-deficient neurons within the same animal. In this animal model, there was a mosaic, where all mice carried a GFP-tagged wild-type MECP2 allele, with the Rett syndrome model animals possessing a null allele on the opposite chromosome (Jaenisch et al., 2004). This configuration allowed us to compare cell to cell variation of chromatin within the same animal, and thus subject to the same developmental and environmental circumstances, but differing in a single gene function. Using this model, we found consistent alterations in chromatin organization using multiple metrics.

4.4.1 Global Disruption of Foci Geometry in MECP2 Mutants

We observed alterations in chromatin geometry in layer2 neurons across animals. Our groupwise analyses spanned four mouse genotypes - two wild-type (CTRL1, CTRL2) and two Mecp2-deficient (RT1, RT2). Despite inherent within-animal variability, statistical tests report that these interactions only occur for comparisons between control-Rett groups. In other words, Rett mice consistently exhibited increased foci volumes and reduced ellipticity compared to control mice.

What is particularly noticeable is that the genotype of the animal had a larger effect than the difference between GFP-positive (WT) and GFP-negative (RT) neurons. This could suggest a cell non-autonomous component to chromatin structure and MECP2 loss. Rett syndrome pathology is not solely the result of cell-autonomous deficits within MECP2-deficient neurons, but also includes substantial non-cell-autonomous contributions from both glial and neuronal populations. Classical studies have shown that MECP2-deficient glia (Ballas et al., 2009; Maezawa and Jin, 2010) can impair the health and function of nearby wild-type neurons. Additionally, secreted factors such as BDNF are disrupted in Rett syndrome (Sampathkumar et al., 2016). Further studies using cell-type-specific conditional knockouts of glia cells or alterations of BDNF would be welcome.

4.4.1 Morphology of Foci and MECP2

Previous studies have demonstrated that MECP2 dosage alters heterochromatin foci shape and number. For example, Ito-Ishida et al. (2020) found that MeCP2-null excitatory-cortical neurons exhibited larger and less elliptical DAPI-dense foci, whereas MeCP2-overexpressing neurons showed smaller, more elongated foci. Similarly, Singleton et al. (2011) reported that MeCP2-deficient neurons fail to undergo typical heterochromatin fusing, resulting in more numerous, smaller chromocenters and abnormal nucleoli.

These observations are not in full agreement with what Ito-Ishida et al. (2020) reported in cortical neurons where ellipticity decreases in MECP2-Null mice. One possible explanation for this discrepancy lies in methodological differences. For instance, Ito-Ishida et al. (2020) did not report significant changes in volume but did observe changes in brightness, potentially due to their use of higher-resolution imaging. In contrast, our imaging setup may have introduced some overestimation in size due to spherical aberration and out-of-focus light, particularly in deeper z-stacks. In Fig S1.G, we see no difference in laser power for thresholding and the cortical neurons in this study were subjected to less variation in microscopic parameters than other neuronal groups, but the possibility remains.

In addition, there is the possibility that the data comes from the distortion of the nucleus. In Fig S1.H, we also do not see a correlation with foci ellipticity and nucleus ellipticity, suggesting the ellipticity is not arising from the physical distortion of the nucleus. However, in Fig S1.I, we see an association with nucleus size, suggesting that some of the effects we observe are related to nucleus size.

In either case, a true difference in ellipticity would support an alternate role of MECP2 in regards to phase-phase formation of chromatin foci. Although the effect size was modest, the consistent increase in ellipticity in MECP2-deficient neurons might reflect the chromatin condensates losing some of their structural cohesion. Rounder foci are generally thought to represent stable, liquid-like condensates that minimize surface tension (Strom et al, 2017). Given that heterochromatin foci are considered membrane-less organelles formed through phase separation, this subtle change in shape could reflect a disruption in the biophysical interactions that underlie phase-phase separation.

In our dataset, we did not detect significant changes in the number of foci per nucleus. However, had such a difference been present, it would have further supported the idea that MECP2 influences fusion dynamics of heterochromatin domains. Singleton et al. (2011) specifically noted a failure of fusion in MECP2-deficient neurons that are dependent on the Methyl-Binding Domain, supporting this possibility. Taken together, future work that tests a model where MECP2 plays a key role in modulating the material properties of heterochromatin is encouraged.

This also raises the question of whether the observed changes - if driven by MECP2 - result from direct interactions between MECP2 and the foci, or are mediated indirectly through intermediate molecular partners. Future biochemical assays and fluorescence recovery after photobleaching (FRAP) could help elucidate the dynamic behavior of MECP2-associated chromatin in live cell imaging contexts (Pantier et al., 2024). An informative follow-up analysis could involve quantifying MECP2 colocalization within chromocenters and with additional nuclear markers, leveraging existing data from the GFP channel. To gain deeper biological insight, this analysis could be expanded using immunofluorescence with antibodies against chromatin-associated proteins, such as heterochromatin protein 1 (HP1α)(Strom et al., 2017), histone modifications (e.g., H3K9me3) (Brero et al., 2005), or markers of transcriptional repression (e.g., NCoR or HDACs) (Strom et al., 2017).

Moreover, Förster resonance energy transfer (FRET) studies would be particularly useful to probe the nanoscale proximity of MECP2 with its molecular partners in situ, providing insight into direct physical interactions within chromatin compartments (Lleres et al., 2009; Hager et al., 2009). The biological understanding would be enhanced if the phase-condensates were directly manipulated, in which treatment similar to such as 1,6-hexanediol—which disrupts weak hydrophobic interactions characteristic of phase-separated condensates—could test the hypothesis that MECP2 contributes to the formation of biomolecular condensates (Duster et al., 2021).

4.5.1 Limitations

It is important to emphasize, however, that these findings, especially the MECP2$^{+/-}$ findings, are preliminary and come with important caveats.

First, the effect sizes were small and observed in a limited sample – the study was constrained by low n (a modest number of animals and cells), meaning statistical power is limited. While the differences were consistent in direction, a larger cohort is needed to confirm significance and generalize to a broader population.

Second, for the *Similarity* assays, we have to consider that the sample size has been artificially inflated by the fact that we have done all possible pairwise comparisons in combination. However, statistics of this kind have been used elsewhere (Cappela et al., 2024).

Third, our spatial analyses lacked internal nuclear landmarks such as the nucleolus or specific chromosomal FISH markers. Without anchoring the orientation of each nucleus, we treated the heterochromatin point cloud in a rotation-invariant manner. This is suitable for automated classification, but it means we cannot easily draw correlations with biological processes. Including such landmarks in future studies could pinpoint which aspect of spatial organization is altered (position, not just size/count)

4.5.2: List of Shortcomings, Hiccups, and Trade-offs (SHiT List)

- Chromatin Staining: DAPI highlights DNA-rich regions but does not distinguish chromatin subtypes. More specific markers for euchromatin and heterochromatin would provide clearer insights into chromatin organization.
- Lack of Neuronal Markers: No specific neuronal type or subtype markers were used. Aside from ACh neurons, only DAPI was used. Therefore it is possible glia were included in the dataset.
- Missing Subtype Resolution: Without antibody-based staining, the precise neuronal subtypes analyzed remain uncertain.
- Low Sample Size: A limited number of mice and nuclei were included, potentially affecting statistical power and generalizability.
- No Soma Staining: Somatic structure was not visualized, making it unclear whether nuclear features reflect changes in the soma.

- Damaged Sample: The cortex from mouse F4 was unintentionally lost due to poor slice preservation.
- Inconsistent Z-Stack Height: Variation in Z-height across stacks may have introduced differences in out-of-focus light and photobleaching.
- Mounting Variability: Sections experienced inconsistent mounting conditions (e.g., slide handling, nail polish sealing, storage time in fridge). While most comparisons were within-slide, some cross-slide variation remains.

4.5.3: Strategies to Improve the Degree of Similarity Metric

- Multiplexing: Incorporating additional molecular channels (e.g., chromatin subtypes, histone marks) would allow for richer spatial comparisons across nuclei.
- Nuclear Interaction Proteins: Metrics such as Iterative Closest Point (ICP) have been applied to 3D protein structure by treating atoms (e.g., carbon, nitrogen, oxygen) as separate channels- similar strategies could be adapted for nuclear organization studies (Ankomah et al., 2020).
- Temporal Expression Patterns: Adding a time dimension through live-cell imaging could reveal how nuclear architecture dynamically changes in response to experimental perturbations.
- Landmark-Based Registration: Future refinements could involve anchoring similarity metrics to subnuclear landmarks (e.g., nucleoli, nuclear lamina) to improve alignment and biological interpretability.

- Improved Imaging Resolution: Advanced microscopy techniques like STORM (Stochastic Optical Reconstruction Microscopy) offer sub-diffraction resolution, enabling more detailed mapping of chromatin structure and nuclear features.

Chapter 5: Conclusion

This thesis set out to quantify the 3D organization of heterochromatin foci across different neuronal cell types using established 3D morphology techniques, as well as novel applications of spatial analysis methods. In terms of morphology, we measured the number, volume, and ellipticity of heterochromatin foci in neurons from the cortex, hippocampus, striatum, and cerebellum. Cerebellar Purkinje neurons stood out as having a greater quantity, larger size, and more ellipticity than compared to other neuron types. Other neuron types had greater variability in their morphological features, but could not be clearly distinguished from each other using these features alone. These morphological differences suggest that certain neurons, like Purkinje cells, have particularly stable and distinct chromatin architectures, while others are more difficult to discriminate.

To better understand how heterochromatin is spatially positioned, we developed and applied two similarity metrics: one measuring morphological overlap of foci (*Morphological Similarity*) and another the spatial arrangement of foci centroids (*Spatial Similarity*). Both of these readouts demonstrate that Purkinje neurons had the highest within-group *Similarity*. By contrast, the cortical, striatal, and hippocampal neurons were less spatially stereotyped and showed more variability within their neuron type group. When comparing between groups, only hippocampal CA1 and striatum neurons were less similar then they are to each other. Overall these results suggest that different cell types have varying levels of rigidity in spatial structure.

We then extended this framework to examine how MECP2 loss of function affects heterochromatin organization. In the Rett mouse model, we compared wild-type and MECP2-deficient neurons within the same mice and found some consistent alterations: foci in MECP2-deficient neurons tended to be larger and slightly more rounded, and both morphological and spatial *Similarity* were reduced compared to wild-type neurons. These findings align with the observations of Ito-Ishida et al. (2020), but whether these results reflect the Loss of Function allele to MECP2, or the MECP2-GFP allele, remains to be determined in future experiments controlling for this factor.

Taken together, these findings provide a foundation for analyzing 3D chromatin arrangements in neuronal nuclei. Future surveys of neurons across the brain that employ more precise neuron-type specificity, and larger sample sizes, are welcome. Additionally, the employment of fluorescent markers for intra-nuclear proteins such as MECP2 and its interacting partners, including various histone modifications, offers the possibility of testing hypotheses related to spatial genome organization and links to neuronal phenotype and function.

Furthermore, extending this work beyond a mouse model of Rett syndrome to include patient-derived models of human diseases offers an opportunity to compare affected individuals with healthy controls, providing insights into the mechanisms underlying disease. Taken together, this work establishes a platform for exploring the 3D genome in neurons and underscores the importance of nuclear architecture in both a basic biological context as well as in neurodevelopmental disorders.

Supplemental

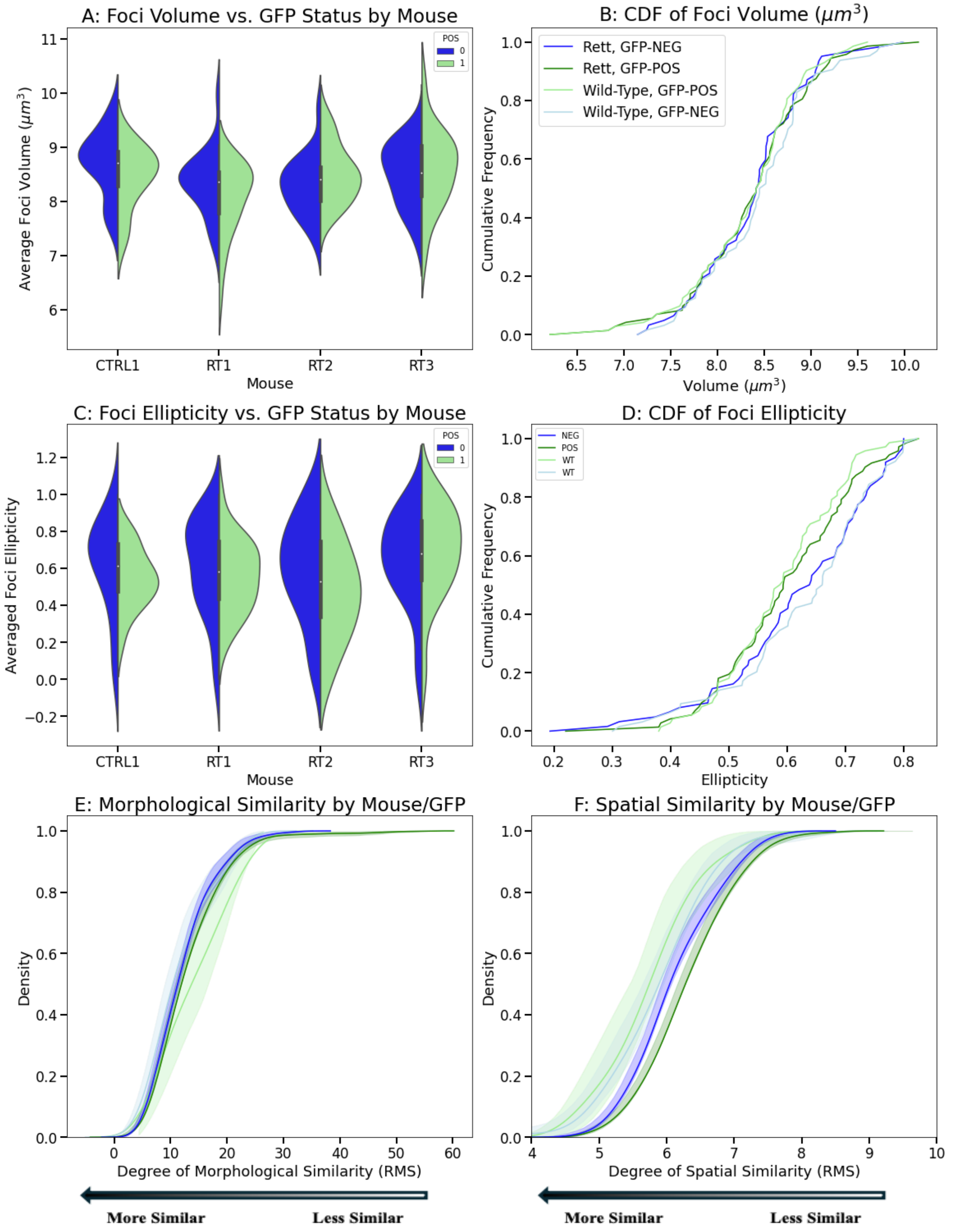
A: Foci Volume vs. GFP Status by Mouse

B: CDF of Foci Volume (μm^3)

C: Foci Ellipticity vs. GFP Status by Mouse

D: CDF of Foci Ellipticity

E: Morphological Similarity by Mouse/GFP

F: Spatial Similarity by Mouse/GFP

Supplemental Figure 1. Preliminary Analysis of Purkinje Neuronal Foci.

Preliminary results evaluating morphological and spatial characteristics of nuclear foci in Purkinje neurons, stratified by GFP status and genotype.

(A) Split-violin plots of average foci volume (μm^3) in GFP-positive (GFP$^+$) vs. GFP-negative (GFP$^-$) nuclei, grouped by individual mouse. CTRL1 represents a wild-type control; RT1–RT3 represent Rett syndrome model mice. Mean ± SD values per mouse: CTRL1 = 8.59 ± 0.59, RT1 = 8.18 ± 0.64, RT2 = 8.41 ± 0.54, RT3 = 8.54 ± 0.64. One-way ANOVA indicated a significant main effect of the mouse ($F = 4.25$, $p = 0.0063$); Tukey HSD showed CTRL1 vs. RT1 was significant ($p = 0.0083$, Bonferroni-corrected $p = 0.0498$).

(B) Cumulative distribution functions (CDFs) of foci volume across genotype and GFP status.

(C) Split-violin plots of average foci ellipticity by mouse and GFP status. Mean ± SD: CTRL1 = 0.61 ± 0.12, RT1 = 0.61 ± 0.11, RT2 = 0.60 ± 0.11, RT3 = 0.60 ± 0.15. No significant differences were detected (one-way ANOVA $F = 0.053$, $p = 0.984$; all Tukey post hoc $p > 0.98$).

(D) CDFs of foci ellipticity corresponding to (C).

(E) Distributions of morphological similarity between nuclei, quantified as root-mean-square (RMS) differences in shape. Lower RMS values indicate greater morphological similarity. Rett GFP$^-$ = 18.85 ± 8.83; Rett GFP$^+$ = 20.80 ± 11.55; WT GFP$^-$ = 17.77 ± 9.97; WT GFP$^+$ = 23.24 ± 11.23. GFP$^+$ nuclei show reduced morphological similarity overall.

(F) Distributions of spatial similarity, quantified as RMS differences in 3D spatial organization. Lower values indicate greater spatial overlap and similarity. Rett GFP$^+$ nuclei show significantly reduced similarity (T-test $p = 2.4 \times 10^{-9}$; Mixed Linear Model: GFP effect $p < 0.001$; GFP - Genotype interaction $p = 0.040$).

This data suggests subtle genotype- and GFP-dependent differences in Purkinje nuclear organization, highlighting the need for more wild-type mice for additional validation.

Supplemental Methods:

S.1 Introduction to Point Sets

In Biology/Neuroscience, most morphological methods involve analysis of 3D image stacks. Typically the image stack will be binarized- where each pixel value will be one of two values representing foreground and background, such as 0 or 1. Measurements can then be directly made on this binarized image mask directly. However, other fields utilize other data structures for morphological analysis, such as Point Clouds.

A point cloud is an array of discrete points in space, where each point is defined by coordinate (x, y, z). To convert an image to a Point Cloud, we can iterate over a binarized image stack and append the coordinates of the foreground. Point Clouds can be visualized using Open Source tools like Blender or Open3D. Many fields use Point Clouds, such as geographical imaging (LIDAR), robotics, and computer animation.

An important distinction of point clouds over image stacks is that they are not constrained by the fixed coordinate frame of a grid. This allows them to be freely rotated without introducing registration artifacts. As an example, if you have two 3D image stacks, where one stack is taken 15 degrees off center of the other, they could not be superimposed without losing data; registration of image stacks is procrustean in nature, artificially forcing an object with continuous curvature into an artificially constructed grid.

S.2 Alignment

When comparing spatial patterns between different samples or conditions, it is often necessary to register (align) the point cloud into a common coordinate system. This superimposition allows direct comparison of spatial dispersion and morphology of entities. In fields that would require precise identification of 3D morphology, such as medical imaging and forensics, 3D Point Clouds and their derivatives have been used to classify ill-defined shapes. For example, it has been used for classifying bones (Akhter et al., 2024) and dental imaging (Zhang et al., 2024).

Superimposition of Point Clouds can be done in various ways. A classic algorithm is Iterative Closest Point (ICP). ICP works by taking two point sets, one for reference and the other for movement. The moveable point cloud is iteratively rotated to minimize the distance to the reference cloud. ICP can achieve very high registration accuracy. A disadvantage of ICP is that it can get “stuck” in a local minima before reaching an accurate alignment. To avoid this, the clouds should already be somewhat oriented.

S.3 Point Cloud Distance Metrics

In conventional bioimage analysis, colocalization metrics quantify how much two labeled structures occupy the same space in a static image. For instance, one might measure the fraction of overlapping voxels/pixels between two fluorescence channels or compute a correlation coefficient of their intensities. Such metrics indicate if two types of signals (say, two proteins or a protein and heterochromatin) tend to be found together.

After point clouds are aligned, we can use quantitative metrics to compare their spatial distribution. This task is analogous to computing the “overlap” or “colocalization”, which represents how much two entities occupy the same space in a static image. An example would be measuring the fraction of overlapping voxels/pixels between two fluorescence channels. However, as said previously, these voxel-based measures are limited to the fixed coordinate frame of the image stack.

Depending on the application different metrics can be used. For example, Root Mean Square (RMS) and Chamfer Distance are highly common and ubiquitous distance functions for spatial data (Ankomah et al., 2020), as well as a loss function in data of arbitrary dimensions.

In this thesis, the term “Similarity” is frequently used and is simply the inverse of “Distance”. This term is favored because Similarity is more intuitive.

S.4 Methods

Images were processed, loaded into Numpy, and interpolated as described in *Methods*. Three-dimensional binary arrays were transformed into an array of 3D coordinates (n, 3), where n represents the number of binary foreground voxels. This transformation was achieved by iterating through each voxel in the 3D array and recording the coordinates of all voxels with a non-zero intensity value. The mean average X, Y, Z coordinate was found and subtracted from the 2D array to “center” the point cloud. Principal Component Analysis (PCA) was performed using the SciPy implementation to estimate a common coordinate system through which to coarsely align Point Clouds. Projection vectors were aligned by projecting point clouds onto the first three principal axes.

An implementation of the Iterative Closest Point (ICP) algorithm was made following the original algorithm (Besl & McKay, 1992) and utilized Singular Value Decomposition (SVD) functions in NumPy. Nearest Neighbours Mean squared error was used as the loss function. To prevent potential shift overflows, a maximum point-to-point distance threshold of 250 units was applied. A KD-tree structure was constructed to identify nearest neighbors efficiently during each ICP iteration. From this, statistics such as the mean and squared mean distances between matched points were computed.

The resulting rotation matrix was converted into a geodesic distance(Crane et al, 2020), providing a scalar measure of rotational difference between nuclear shapes for interpretability and quantitative comparison.

S.5: Visualization and Analysis

Final point clouds and surface reconstructions were visualized using Open3D (v0.18.0) and/or Blender to assess shape alignment and transformation accuracy. All data was analyzed using the Python programming language. Geodesic distances above 1 radian (60 degrees) were excluded. Each figure was created in a different Python script, in a different folder.

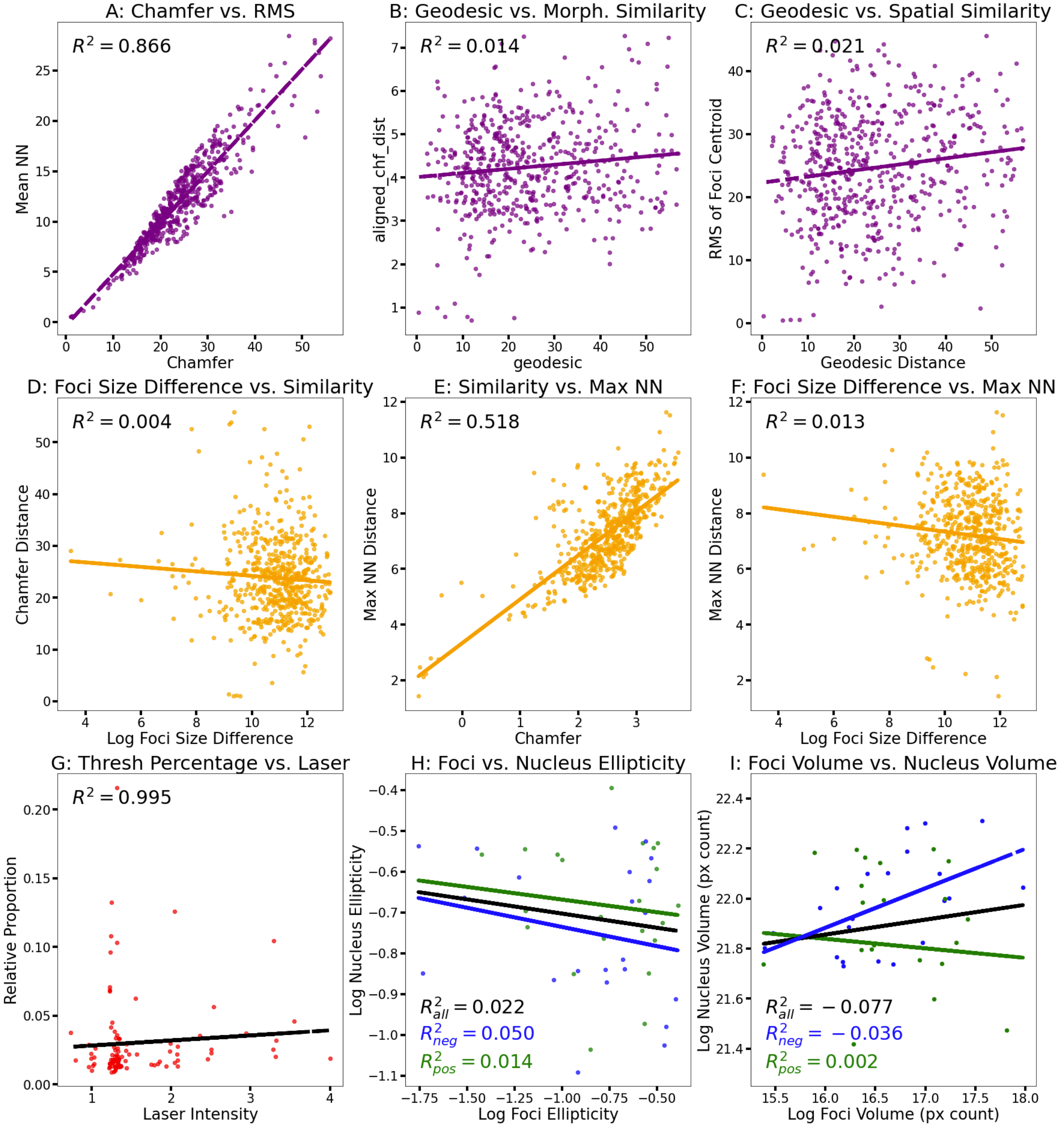

Fig S2: Select Factors That Could Impact Metrics

A) Comparison with Alternate Distance Metric: For each pair of aligned point clouds, we computed Root Mean Square (RMS) and Chamfer distances. Results showed a high correlation (Pearson *r* = 0.93, *p* < 1e-245; Spearman *r* = 0.92, *p* < 0.0001), indicating these metrics capture comparable features of shape similarity.

B) Geodesic Rotation vs. *Morphological Similarity*: the geodesic rotation (i.e., how much ICP rotated the cloud during alignment) against the final RMS score. A weak correlation was observed (Pearson $r = 0.12$, $p = 0.0047$; Spearman $r = 0.07$, $p = 0.0971$). These results suggest that large rotations do not systematically bias the similarity measurement.

C) Geodesic Rotation vs. *Spatial Similarity*: the geodesic rotation (i.e., how much ICP rotated the cloud during alignment) against the final RMS score. A weak correlation was observed (Pearson $r = 0.15$, $p = 0.0006$; Spearman $r = 0.13$, $p = 0.0022$). These results suggest that large rotations do not systematically bias the similarity measurement.

D) Foci Size Difference vs. *Similarity*: Differences in total foci volume between nuclei did not significantly correlate with similarity scores (Pearson $r = –0.065$, $p = 0.12$; Spearman $r = –0.059$, $p = 0.17$).

E) Similarity vs. Max Nearest Neighbour Distance: similarity scores were correlated with the maximum nearest neighbor distance (Pearson $r = 0.72$, $p = 8.6e–91$; Spearman $r = 0.69$, $p < 0.0001$), suggesting that high similarity is associated with more uniformly distributed local distances.

F) A weak negative correlation was found (Pearson $r = –0.12$, $p = 0.0065$; Spearman $r = –0.13$, $p = 0.0020$), indicating slight influence of foci volume imbalance on spatial proximity measures.

G) Scatterplot of laser intensity vs. threshold class proportions in Purkinje neurons. A slight jitter was applied for visualization.

H) Foci vs. Nucleus Ellipticity. Trendlines for GFP POS, GFP NEG, and combined (black) cortical neurons shown.

I) Foci Volume vs. Nucleus Volume.

S.7 Self Similarity: Initial Rotation

To gauge the method's rotational limit, a reference point cloud was rotated around the x, y, and z axes by known angles. Results were averaged for each incremental geodesic distance, but were made from separate rotations for each axis. Below about 60° of rotation, the algorithm consistently recovered the correct orientation, but beyond this threshold, it occasionally failed to re-align the identical Point Cloud.

Takeaways:

- **Robust Up to 60 Degrees**: Below about 60° of rotation, ICP reliably converged back to the correct orientation, with minimal final misalignment.
- **Failure Beyond 60 Degrees**: At larger angles, ICP sometimes became trapped in local minima, causing poor alignment. For this reason, comparisons where the initial orientation exceeded 60° were either excluded or inspected.

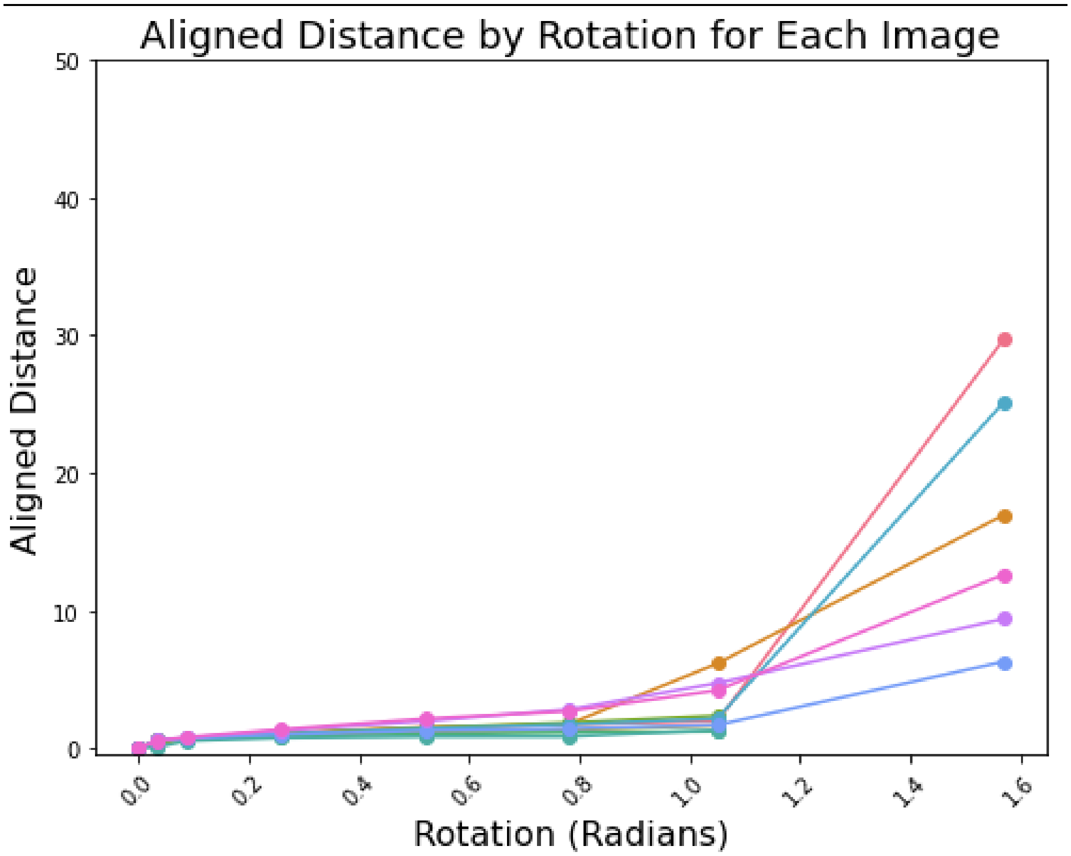

Figure S3: Self-Similarity and Initial Rotation Tolerance of ICP.

S.8 Self Similarity: Noise Sensitivity

To evaluate how progressively larger deviations influence the **Degree of Similarity** metric, artificial “salt and pepper” noise was iteratively introduced into binarized images prior to point cloud generation. The noise level was incremented from 0% to 5% of total voxels. The resulting Root Mean Square (RMS) distance between the noise-altered and unaltered point clouds was measured. Takeaways:

1. **Dose-Dependent Increase**: As more voxels were modified by noise, the RMS distance increased in a dose dependent manner. Relatively small amounts of noise (1–2%) triggered measurable increases in dissimilarity.
2. **Switchlike Plateau**: Beyond approximately 3% noise, the RMS distance began to plateau.
3. **Different Plateau Values**: The exact plateau value for the RMS distance varied slightly between Point Clouds.

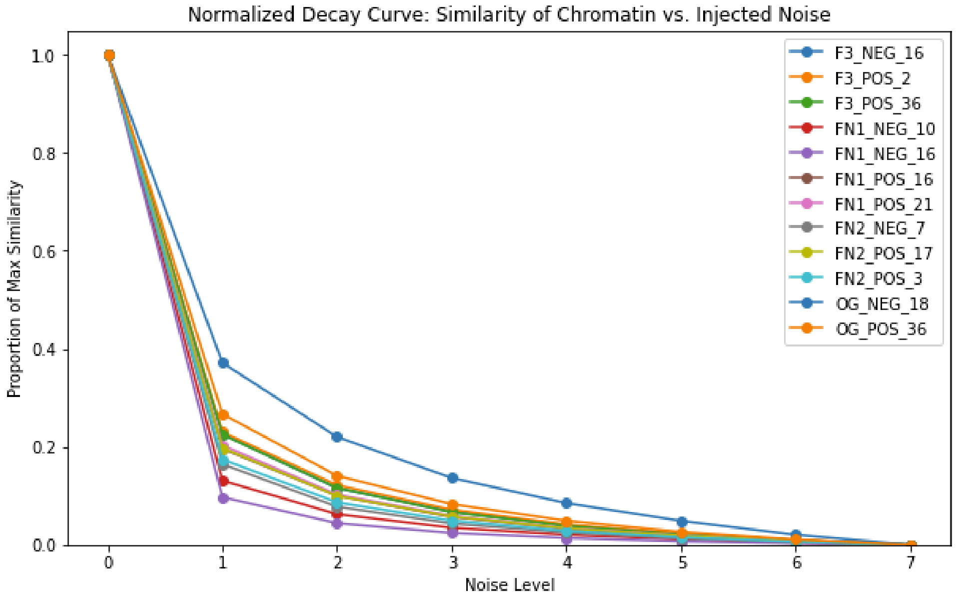

Figure S4: Sensitivity of Self-*Similarity* to Voxel Noise.

2.3 Self Similarity: Random Scrambling of Foci:

To examine different positioning of foci, threshold foci were randomly displaced (with a uniform distribution) within the spatial boundaries of their nucleus. Three “scrambled” Point Clouds were made for each test Point Cloud and plotted. Takeaways:

1. **High Variability:** Each “scrambled” Point Cloud has variable difference in RMS.
2. **Spatial Conformation Matters**: scrambled Point Clouds are impacted.

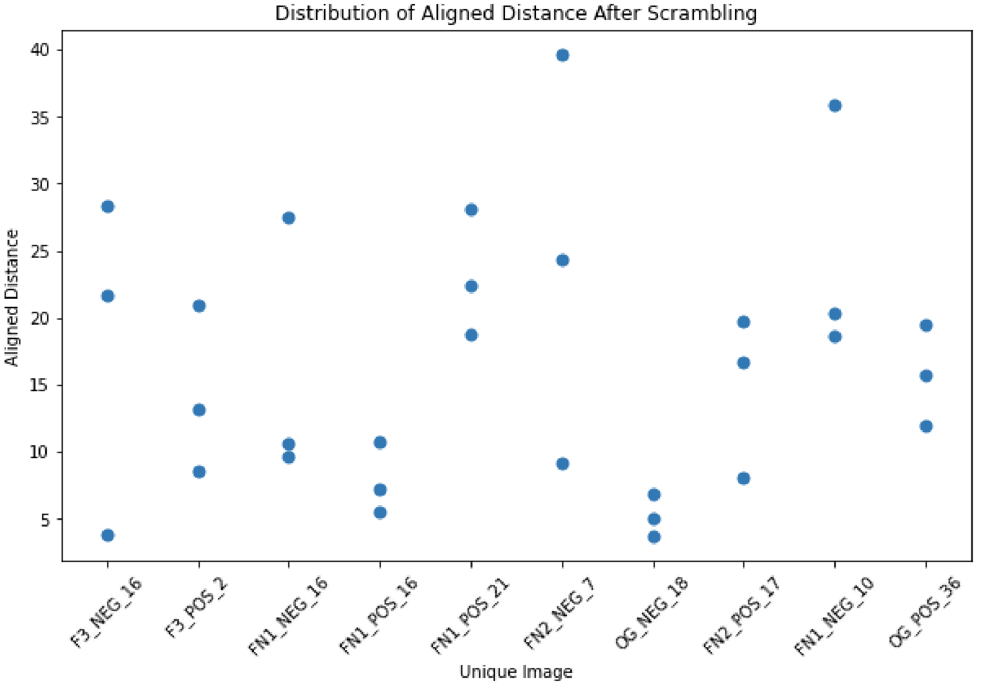

Figure S5: Sensitivity of Self-*Similarity* to Random Scrambling of Foci Positions

References

Abewe, H., A. Richey, J. M. Vahrenkamp, M. Ginley-Hidinger, C. M. Rush, N. Kitchen, X. Zhang and J. Gertz. 2025. Estrogen-induced chromatin looping changes identify a subset of functional regulatory elements. bioRxiv 2024.06.12.598690.

Agarwal, N., A. Becker, K. L. Jost, S. Haase, B. K. Thakur, A. Brero, T. Hardt, S. Kudo, H. Leonhardt and M. C. Cardoso. 2011. MeCP2 Rett mutations affect large scale chromatin organization. Human Molecular Genetics 20: 4187–4195.

Aguirre-Lavin, T., P. Adenot, A. Bonnet-Garnier, G. Lehmann, R. Fleurot, C. Boulesteix, P. Debey and N. Beaujean. 2012a. 3D-FISH analysis of embryonic nuclei in mouse highlights several abrupt changes of nuclear organization during preimplantation development. BMC Developmental Biology 12: 30.

Akhmanova, A., T. Verkerk, A. Langeveld, F. Grosveld and N. Galjart. 2000. Characterisation of transcriptionally active and inactive chromatin domains in neurons. Journal of Cell Science 113: 4463–4474.

Arzate-Mejia, R. G. and I. M. Mansuy. 2023. Remembering through the genome: the role of chromatin states in brain functions and diseases. Transl Psychiatry 13: 1–11.

Ankomah, P., Vangorp, P., Behera, A., & Liu, Y. 2020. Tagged-ICP: An Iterative Closest Point Algorithm with Metadata Knowledge for Improved Matching of 3D Protein Structures. Proceedings of the Irish Machine Vision and Image Processing Conference 2020, 37–44.

Baldi, S., P. Korber and P. B. Becker. 2020. Beads on a string—nucleosome array arrangements and folding of the chromatin fiber. Nat Struct Mol Biol 27: 109–118.

Baltanás, F. C., I. Casafont, V. Lafarga, E. Weruaga, J. R. Alonso, M. T. Berciano and M. Lafarga. 2011. Purkinje Cell Degeneration in pcd Mice Reveals Large Scale Chromatin Reorganization and Gene Silencing Linked to Defective DNA Repair. J Biol Chem 286: 28287–28302.

Bannister, A. J. and T. Kouzarides. 2011. Regulation of chromatin by histone modifications. Cell Res 21: 381–395.

Bharadwaj, R., C. J. Peter, Y. Jiang, P. Roussos, A. Vogel-Ciernia, E. Y. Shen, A. C. Mitchell, W. Mao, C. Whittle, A. Dincer, et al.. 2014. Conserved higher-order chromatin regulates NMDA receptor gene expression and cognition. Neuron 84: 997–1008.

Bogolyubov, D. S. 2018. Chapter One - Karyosphere (Karyosome): A Peculiar Structure of the Oocyte Nucleus. In: International Review of Cell and Molecular Biology (L. Galluzzi, ed), pp. 1–48. Academic Press.

Boettiger, A. N., B. Bintu, J. R. Moffitt, S. Wang, B. J. Beliveau, G. Fudenberg, M. Imakaev, L. A. Mirny, C. Wu and X. Zhuang. 2016. Super-resolution imaging reveals distinct chromatin folding for different epigenetic states. Nature 529: 418–422.

Boeynaems, S., S. Alberti, N. L. Fawzi, T. Mittag, M. Polymenidou, F. Rousseau, J. Schymkowitz, J. Shorter, B. Wolozin, L. Van Den Bosch, et al.. 2018. Protein Phase Separation: A New Phase in Cell Biology. Trends Cell Biol 28: 420–435.

Brändle, F., B. Frühbauer and M. Jagannathan. 2022. Principles and functions of pericentromeric satellite DNA clustering into chromocenters. Seminars in Cell & Developmental Biology 128: 26–39.

Bortle, K. V. and V. G. Corces. 2012. Nuclear Organization and Genome Function. Annu Rev Cell Dev Biol 28: 163–187.

Brero, A., H. P. Easwaran, D. Nowak, I. Grunewald, T. Cremer, H. Leonhardt and M. C. Cardoso. 2005a. Methyl CpG-binding proteins induce large-scale chromatin reorganization during terminal differentiation. J Cell Biol 169: 733–743.

Cai, L. and G. G. Wang. n.d. Through the lens of phase separation: intrinsically unstructured protein and chromatin looping. Nucleus 14: 2179766.

Cappella, A., A. Palamenghi, R. Solazzo, D. Mazzarelli, D. Gibelli, C. Sforza and C. Cattaneo. 2024. An exclusionary screening method based on 3D morphometric features to sort commingled atlases and axes. Sci Rep 14: 13149.

Cembrowski, M. S., J. L. Bachman, L. Wang, K. Sugino, B. C. Shields and N. Spruston. 2016. Spatial Gene-Expression Gradients Underlie Prominent Heterogeneity of CA1 Pyramidal Neurons. Neuron 89: 351–368.

Crane, K., M. Livesu, E. Puppo and Y. Qin. 2020. A Survey of Algorithms for Geodesic Paths and Distances. arXiv.

Cremer, M., V. J. Schmid, F. Kraus, Y. Markaki, I. Hellmann, A. Maiser, H. Leonhardt, S. John, J. Stamatoyannopoulos and T. Cremer. 2017. Initial high-resolution microscopic mapping of active and inactive regulatory sequences proves non-random 3D arrangements in chromatin domain clusters. Epigenetics & Chromatin 10: 39.

Clowney, E. J., M. A. LeGros, C. P. Mosley, F. G. Clowney, E. C. Markenskoff-Papadimitriou, M. Myllys, G. Barnea, C. A. Larabell and S. Lomvardas. 2012. Nuclear Aggregation of Olfactory Receptor Genes Governs Their Monogenic Expression. Cell 151: 724–737.

Del Monte, U. 2006. The puzzle of ploidy of Purkinje neurons. Cerebellum 5: 23–26.

Das, S. and N. Ramanan. 2023. Region-specific heterogeneity in neuronal nuclear morphology in young, aged and in Alzheimer’s disease mouse brains. Front Cell Dev Biol 11: 1032504.

Dong, P., L. Song, J. Bendl, R. Misir, Z. Shao, J. Edelstien, D. A. Davis, V. Haroutunian, W. K. Scott, S. Acker, et al.. 2024. A multi-regional human brain atlas of chromatin accessibility and gene expression facilitates promoter-isoform resolution genetic fine-mapping. Nat Commun 15: 10113.

Düster, R., Kaltheuner, I. H., Schmitz, K., & Schmitz, K. M. (2021). The elusive landscape of DNA methylation maintenance during replication. Nucleic Acids Research, 49(15), 8420–8439. DOI: 10.1093/nar/gkab608. [Online] Available: https://www.ncbi.nlm.nih.gov/pmc/articles/PMC7948595/\

Favaro, R., M. Valotta, A. L. M. Ferri, E. Latorre, J. Mariani, C. Giachino, C. Lancini, V. Tosetti, S. Ottolenghi, V. Taylor, et al.. 2009. Hippocampal development and neural stem cell maintenance require Sox2-dependent regulation of Shh. Nat Neurosci 12: 1248–1256.

Falk, M., Y. Feodorova, N. Naumova, M. Imakaev, B. R. Lajoie, H. Leonhardt, B. Joffe, J. Dekker, G. Fudenberg, I. Solovei, et al.. 2019. Heterochromatin drives compartmentalization of inverted and conventional nuclei. Nature 570: 395–399.

Feodorova, Y., M. Falk, L. A. Mirny and I. Solovei. 2020. Viewing Nuclear Architecture through the Eyes of Nocturnal Mammals. Trends in Cell Biology 30: 276–289.

Fischer, E. F., G. Pilarczyk and M. Hausmann. 2023. Microscopic Analysis of Heterochromatin, Euchromatin and Cohesin in Cancer Cell Models and under Anti-Cancer Treatment. Curr Issues Mol Biol 45: 8152–8172.

Fischer, E. F., G. Pilarczyk and M. Hausmann. 2023. Microscopic Analysis of Heterochromatin, Euchromatin and Cohesin in Cancer Cell Models and under Anti-Cancer Treatment. Curr Issues Mol Biol 45: 8152–8172.

Fortuny, A., A. Chansard, P. Caron, O. Chevallier, O. Leroy, O. Renaud and S. E. Polo. 2021. Imaging the response to DNA damage in heterochromatin domains reveals core principles of heterochromatin maintenance. Nat Commun 12: 2428.

Fujita, Y., S. R. Pather, G. Ming and H. Song. 2022. 3D spatial genome organization in the nervous system: From development and plasticity to disease. Neuron 110: 2902–2915.

García-Cabezas, M. Á., H. Barbas and B. Zikopoulos. 2018. Parallel Development of Chromatin Patterns, Neuron Morphology, and Connections: Potential for Disruption in Autism. Front Neuroanat 12: 70.

Good, K. V., J. B. Vincent and J. Ausió. 2021. MeCP2: The Genetic Driver of Rett Syndrome Epigenetics. Front Genet 12: 620859.

Grabowska, A., H. Sas-Nowosielska, B. Wojtas, D. Holm-Kaczmarek, E. Januszewicz, Y. Yushkevich, I. Czaban, P. Trzaskoma, K. Krawczyk, B. Gielniewski, et al.. 2022.

Activation-induced chromatin reorganization in neurons depends on HDAC1 activity. Cell Reports 38: 110352.

Georgel, P. T., R. A. Horowitz-Scherer, N. Adkins, C. L. Woodcock, P. A. Wade and J. C. Hansen. 2003. Chromatin compaction by human MeCP2. Assembly of novel secondary chromatin structures in the absence of DNA methylation. J Biol Chem 278: 32181–32188.

Gulino, G. M., F. Bruno, V. Sturiale, D. Brancato, D. Ragusa, S. Tosi, S. Saccone and C. Federico. 2021. From FISH to Hi-C: The Chromatin Architecture of the Chromosomal Region 7q36.3, Frequently Rearranged in Leukemic Cells, Is Evolutionary Conserved. Int J Mol Sci 22: 2338.

Janssen, A., S. U. Colmenares and G. H. Karpen. 2018. Heterochromatin: Guardian of the Genome. Annu. Rev. Cell Dev. Biol. 34: 265–288.

Hager, G. L., McNally, J. G., & Misteli, T. 2009. Transcription dynamics. Molecular Cell. 35(6): 741–753. DOI: 10.1016/j.molcel.2009.09.005. [Online] Available: https://www.ncbi.nlm.nih.gov/pmc/articles/PMC6326382/

Hirano, T. 2013. Long-term depression and other synaptic plasticity in the cerebellum. Proc Jpn Acad Ser B Phys Biol Sci 89: 183–195.

Hirayama, T., Y. Kadooka, E. Tarusawa, S. Saitoh, H. Nakayama, N. Hoshino, S. Nakama, T. Fukuishi, Y. Kawanishi, H. Umeshima, et al.. 2022. CTCF loss induces giant lamellar bodies in Purkinje cell dendrites. Acta Neuropathol Commun 10: 172.

Horowitz, J. M. and B. A. Horwitz. 2019. Extreme Neuroplasticity of Hippocampal CA1 Pyramidal Neurons in Hibernating Mammalian Species. Front. Neuroanat. 13.

Hoxha, E., F. Tempia, P. Lippiello and M. C. Miniaci. 2016. Modulation, Plasticity and Pathophysiology of the Parallel Fiber-Purkinje Cell Synapse. Front Synaptic Neurosci 8: 35.

Hu, B., H. Won, W. Mah, R. B. Park, B. Kassim, K. Spiess, A. Kozlenkov, C. A. Crowley, S. Pochareddy, Y. Li, et al.. 2021. Neuronal and glial 3D chromatin architecture informs the cellular etiology of brain disorders. Nat Commun 12: 3968.

Takizawa, T. and E. Meshorer. 2008. Chromatin and nuclear architecture in the nervous system. Trends in Neurosciences 31: 343–352.

Ibarra, I. L., V. S. Ratnu, L. Gordillo, I.-Y. Hwang, L. Mariani, K. Weinand, H. M. Hammarén, J. Heck, M. L. Bulyk, M. M. Savitski, et al.. 2022. Comparative chromatin accessibility upon BDNF stimulation delineates neuronal regulatory elements. Mol Syst Biol 18: e10473.

Ito, S., A. Magalska, M. Alcaraz-Iborra, J. P. Lopez-Atalaya, V. Rovira, B. Contreras-Moreira, M. Lipinski, R. Olivares, J. Martinez-Hernandez, B. Ruszczycki, et al.. 2014. Loss of neuronal 3D chromatin organization causes transcriptional and behavioural deficits related to serotonergic dysfunction. Nat Commun 5: 4450.

Ip, J. P. K., N. Mellios and M. Sur. 2018. Rett syndrome: insights into genetic, molecular and circuit mechanisms. Nat Rev Neurosci 19: 368–382.

Ito-Ishida, A., S. A. Baker, R. V. Sillitoe, Y. Sun, J. Zhou, Y. Ono, J. Iwakiri, M. Yuzaki and H. Y. Zoghbi. 2020. MeCP2 Levels Regulate the 3D Structure of Heterochromatic Foci in Mouse Neurons. J Neurosci 40: 8746–8766.

Kepecs, A. and G. Fishell. 2014. Interneuron cell types are fit to function. Nature 505: 318–326.

Kandel ER, Koester JD, Mack SH, Siegelbaum SA. 2021. Principles of Neural Science. 6th ed. New York (NY): McGraw-Hill Education.

Luikenhuis, S., E. Giacometti, C. F. Beard and R. Jaenisch. 2004. Expression of MeCP2 in postmitotic neurons rescues Rett syndrome in mice. Proc Natl Acad Sci U S A 101: 6033–6038.

Lyons, D. B., A. Magklara, T. Goh, S. C. Sampath, A. Schaefer, G. Schotta and S. Lomvardas. 2014. Heterochromatin-Mediated Gene Silencing Facilitates the Diversification of Olfactory Neurons. Cell Reports 9: 884–892.

Lyst, M. J. and A. Bird. 2015. Rett syndrome: a complex disorder with simple roots. Nat Rev Genet 16: 261–275.

Li, C. H., E. L. Coffey, A. Dall'Agnese, N. M. Hannett, X. Tang, J. E. Henninger, J. M. Platt, O. Oksuz, A. V. Zamudio, L. K. Afeyan, et al.. 2020. MeCP2 links heterochromatin condensates and neurodevelopmental disease. Nature 586: 440–444.

Li, Y., V. Agrawal, R. K. A. Virk, E. Roth, W. S. Li, A. Eshein, J. Frederick, K. Huang, L. Almassalha, R. Bleher, et al.. 2022. Analysis of three-dimensional chromatin packing domains by chromatin scanning transmission electron microscopy (ChromSTEM). Sci Rep 12: 12198.

Ma, R., Y. Zhang, J. Zhang, P. Zhang, Z. Liu, Y. Fan, H.-T. Wang, Z. Zhang and B. Zhu. 2024. Targeting pericentric non-consecutive motifs for heterochromatin initiation. Nature 631: 678–685.

Oey, N. E., H. W. Leung, R. Ezhilarasan, L. Zhou, R. W. Beuerman, H. M. A. VanDongen and A. M. J. VanDongen. 2015. A Neuronal Activity-Dependent Dual Function Chromatin-Modifying Complex Regulates Arc Expression. eNeuro 2.

Martou, G. and U. De Boni. 2000. Nuclear Topology of Murine, Cerebellar Purkinje Neurons: Changes as a Function of Development. Experimental Cell Research 256: 131–139.

McKiernan, E. C. and D. F. Marrone. 2017. CA1 pyramidal cells have diverse biophysical properties, affected by development, experience, and aging. PeerJ 5: e3836.

Mansisidor, A. R. and V. I. Risca. n.d. Chromatin accessibility: methods, mechanisms, and biological insights. Nucleus 13: 236–276.

Montavon, T., N. Shukeir, G. Erikson, B. Engist, M. Onishi-Seebacher, D. Ryan, Y. Musa, G. Mittler, A. G. Meyer, C. Genoud, et al.. 2021. Complete loss of H3K9 methylation dissolves mouse heterochromatin organization. Nat Commun 12: 4359.

Nielsen, J. V., M. Thomassen, K. Møllgård, J. Noraberg and N. A. Jensen. 2014. Zbtb20 Defines a Hippocampal Neuronal Identity Through Direct Repression of Genes That Control Projection Neuron Development in the Isocortex. Cerebral Cortex 24: 1216–1229.

Nishi, A., M. Kuroiwa and T. Shuto. 2011b. Mechanisms for the Modulation of Dopamine D1 Receptor Signaling in Striatal Neurons. Front Neuroanat 5: 43.

Packiaraj, J. and J. Thakur. 2024. DNA satellite and chromatin organization at mouse centromeres and pericentromeres. Genome Biology 25: 52.

Pantier, R., M. Brown, S. Han, K. Paton, S. Meek, T. Montavon, N. Shukeir, T. McHugh, D. A. Kelly, T. Hochepied, et al.. 2024. MeCP2 binds to methylated DNA independently of phase separation and heterochromatin organisation. Nat Commun 15: 3880.

Padeken, J. and P. Heun. 2014. Nucleolus and nuclear periphery: Velcro for heterochromatin. Current Opinion in Cell Biology 28: 54–60.

Pinheiro, I., R. Margueron, N. Shukeir, M. Eisold, C. Fritzsch, Florian M. Richter, G. Mittler, C. Genoud, S. Goyama, M. Kurokawa, et al.. 2012. Prdm3 and Prdm16 are H3K9me1 Methyltransferases Required for Mammalian Heterochromatin Integrity. Cell 150: 948–960.

Pinheiro, I., R. Margueron, N. Shukeir, M. Eisold, C. Fritzsch, Florian M. Richter, G. Mittler, C. Genoud, S. Goyama, M. Kurokawa, et al.. 2012. Prdm3 and Prdm16 are H3K9me1 methyltransferases required for mammalian heterochromatin integrity. Cell 150: 948–960.

Qureshi, I. A. and M. F. Mehler. 2014. An evolving view of epigenetic complexity in the brain. Phil. Trans. R. Soc. B 369: 20130506.

Quiquempoix, M., S. L. Fayad, K. Boutourlinsky, N. Leresche, R. C. Lambert and T. Bessaih. 2018. Layer 2/3 Pyramidal Neurons Control the Gain of Cortical Output. Cell Rep 24: 2799-2807.e4.

Robles, R. M., E. Domínguez-Sala, S. Martínez and E. Geijo-Barrientos. 2020. Layer 2/3 Pyramidal Neurons of the Mouse Granular Retrosplenial Cortex and Their Innervation by Cortico-Cortical Axons. Front. Neural Circuits 14.

Rozo, J. A., I. Martínez-Gallego and A. Rodríguez-Moreno. 2024. Cajal, the neuronal theory and the idea of brain plasticity. Front. Neuroanat. 18: 1331666.

Schindelin, J., I. Arganda-Carreras, E. Frise, V. Kaynig, M. Longair, T. Pietzsch, S. Preibisch, C. Rueden, S. Saalfeld, B. Schmid, et al.. 2012b. Fiji: an open-source platform for biological-image analysis. Nat Methods 9: 676–682.

Schor, I. E., N. Rascovan, F. Pelisch, M. Alló and A. R. Kornblihtt. 2009. Neuronal cell depolarization induces intragenic chromatin modifications affecting NCAM alternative splicing. Proc. Natl. Acad. Sci. U.S.A. 106: 4325–4330.

Shakoori, A. R. 2017. Fluorescence In Situ Hybridization (FISH) and Its Applications. Chromosome Structure and Aberrations 343–367.

Smith, Z. D. and A. Meissner. 2013. DNA methylation: roles in mammalian development. Nat Rev Genet 14: 204–220.

Schmidt, A., J. Frei, A. Poetsch, A. Chittka, H. Zhang, C. Aßmann, A. Lehmkuhl, U.-M. Bauer, U. A. Nuber and M. C. Cardoso. 2022. MeCP2 heterochromatin organization is modulated by arginine methylation and serine phosphorylation. Front. Cell Dev. Biol. 10.

Schmid, V. J., M. Cremer and T. Cremer. 2017. Quantitative analyses of the 3D nuclear landscape recorded with super-resolved fluorescence microscopy. Methods 123: 33–46.

Strom, A. R., A. V. Emelyanov, M. Mir, D. V. Fyodorov, X. Darzacq and G. H. Karpen. 2017. Phase separation drives heterochromatin domain formation. Nature 547: 241–245.

Solovei, I., A. S. Wang, K. Thanisch, C. S. Schmidt, S. Krebs, M. Zwerger, T. V. Cohen, D. Devys, R. Foisner, L. Peichl, et al.. 2013. LBR and Lamin A/C Sequentially Tether Peripheral Heterochromatin and Inversely Regulate Differentiation. Cell 152: 584–598.

Song, C., Y. Feodorova, J. Guy, L. Peichl, K. L. Jost, H. Kimura, M. C. Cardoso, A. Bird, H. Leonhardt, B. Joffe, et al.. 2014. DNA methylation reader MECP2: cell type- and differentiation stage-specific protein distribution. Epigenetics & Chromatin 7: 17.

Wei, C.-L., S. K. Nicolis, Y. Zhu and M. Pagin. 2019. Sox2-Dependent 3D Chromatin Interactomes in Transcription, Neural

Stem Cell Proliferation and Neurodevelopmental Diseases. J Exp Neurosci 13: 1179069519868224.

Ulicna, K., L. T. L. Ho, C. J. Soelistyo, N. J. Day and A. R. Lowe. 2022. Convolutional Neural Networks for Classifying Chromatin Morphology in Live-Cell Imaging. In: Chromosome Architecture: Methods and Protocols (M. C. Leake, ed), pp. 17–30. Springer US, New York, NY.

Vadakkan, Kunjumon I., B. Li and U. De Boni. 2006. Trend towards varying combinatorial centromere association in morphologically identical clusters in Purkinje neurons. Cell chromosome 5: 1.

Weiler, S., D. Guggiana Nilo, T. Bonhoeffer, M. Hübener, T. Rose and V. Scheuss. 2023. Functional and structural features of L2/3 pyramidal cells continuously covary with pial depth in mouse visual cortex. Cerebral Cortex 33: 3715–3733.

Zagirova, D., A. Kononkova, N. Vaulin and E. Khrameeva. 2024. From compartments to loops: understanding the unique chromatin organization in neuronal cells. Epigenetics & Chromatin 17: 18.

Zhang, H., W. Qin, H. Romero, H. Leonhardt and M. C. Cardoso. n.d. Heterochromatin organization and phase separation. Nucleus 14: 2159142.